The earliest phases of high-mass star formation: the NGC 6334-NGC 6357 complex

D. Russeil, Annie Zavagno, F. Motte, N. Schneider, Sylvain Bontemps, A. J. Walsh

A&A 515, A55 (2010)
DOI: 10.1051/0004-6361/200913632

Astronomy & Astrophysics

The earliest phases of high-mass star formation: the NGC 6334-NGC 6357 complex⋆,⋆⋆,⋆⋆⋆

D. Russeil[1], A. Zavagno[1], F. Motte[2], N. Schneider[2], S. Bontemps[3], and A. J. Walsh[4]

[1] Laboratoire d'Astrophysique de Marseille - UMR 6110, CNRS - Université de Provence, 13388 Marseille Cedex 13, France
e-mail: delphine.russeil@oamp.fr
[2] Laboratoire AIM, CEA/DSM - INSU/CNRS - Université Paris Diderot, IRFU/Service d'Astrophysique, CEA-Saclay, 91191 Gif-sur-Yvette Cedex, France
[3] Laboratoire d'Astrophysiaue de Bordeaux, OASU - UMR 5804, CNRS - Université de Bordeaux 1, 2 rue de l'Observatoire, BP 89, 33270 Floirac, France
[4] Centre for Astronomy, School of Engineering and Physical Sciences, James Cook University, Townsville, QLD, 4811, Australia

Received 10 November 2009 / Accepted 11 February 2010

ABSTRACT

Context. Our knowledge of high-mass star formation has been mainly based on follow-up studies of bright sources found by *IRAS*, and has thus been incomplete for its earliest phases, which are inconspicuous at infrared wavelengths. With a new generation of powerful bolometer arrays, unbiased large-scale surveys of nearby high-mass star-forming complexes now search for the high-mass analog of low-mass cores and class 0 protostars.
Aims. Following the pioneering study of Cygnus X, we investigate the star-forming region NGC 6334–NGC 6357 (~1.7 kpc).
Methods. We study the complex NGC 6334–NGC 6357 in an homogeneous way following the previous work of Motte and collaborators. We used the same method to extract the densest cores which are the most likely sites for high-mass star formation. We analyzed the SIMBA/SEST 1.2 mm data presented in Munoz and coworkers, which covers all high-column density areas ($A_v \geq 15$ mag) of the NGC 6334–NGC 6357 complex and extracted dense cores following the method used for Cygnus X. We constrain the properties of the most massive dense cores ($M > 100\ M_\odot$) using new molecular line observations (as SiO, N_2H^+,$H^{13}CO^+$, HCO^+ (1-0) and CH_3CN) with Mopra and a complete cross-correlation with infrared databases (*MSX*, GLIMPSE, MIPSGAL) and literature.
Results. We extracted 163 massive dense cores of which 16 are more massive than 200 $M_\odot$. These high-mass dense cores have a typical *FWHM* size of 0.37 pc, an average mass of $M \sim 600\ M_\odot$, and a volume-averaged density of $\sim 1.5 \times 10^5$ cm^{-3}. Among these massive dense cores, 6 are good candidates for hosting high-mass infrared-quiet protostars, 9 cores are classified as high-luminosity infrared protostars, and we find only one high-mass starless clump (~0.3 pc, $\sim 4 \times 10^4$ cm^{-3}) that is gravitationally bound.
Conclusions. Since our sample is derived from a single molecular complex and covers every embedded phase of high-mass star formation, it provides a statistical estimate of the lifetime of massive stars. In contrast to what is found for low-mass class 0 and class I phases, the infrared-quiet protostellar phase of high-mass stars may last as long as their more well known high-luminosity infrared phase. As in Cygnus X, the statistical lifetime of high-mass protostars is shorter than found for nearby, low-mass star-forming regions which implies that high-mass pre-stellar and protostellar cores are in a dynamic state, as expected in a molecular cloud where turbulent and/or dynamical processes dominate.

Key words. dust, extinction – H II regions – stars: formation – radio continuum: ISM – submillimeter: ISM – radio lines: general

1. Introduction

High-mass (O- or B-type) stars play a major role in the energy budget and enrichment of galaxies, but their formation remains poorly understood. High-mass stars probably form in massive dense cores by the powerful accretion of gas onto a protostellar embryo (e.g. Beuther & Schilke 2004). However, the physical origin of these high accretion rates remains unclear with multiple mechanisms proposed including a high degree of turbulence (McKee & Tan 2002), converging flows (Heitsch et al. 2008), cloud collisions (Bonnell & Bate 2002), and competitive accretion on large scales (Bonnell et al. 2006).

From a purely observational point of view, the evolutionary sequence leading from clouds to OB stars is far from being well constrained. For instance, the existence and lifetime of the infrared (IR)-quiet phase analog to low-mass class 0 protostars and pre-stellar cores for high-mass stars is still a matter of debate (Motte et al. 2007). Moreover, the exact ordering and overlap of the different phases/diagnostics (pre-stellar, cold/infrared-quiet protostar, hot core, $OH/H_2O/CH_3OH$ masers, warm/infrared-bright sources, HMPOs, hypercompact H II, UCH II regions) needs to be fully determined. Therefore, it is of crucial importance to build representative and unbiased samples of high-mass pre-stellar and protostellar objects, in large, nearby, high-mass star formation complexes.

(Sub)millimeter continuum mapping is the perfect tool for systematically searching the earliest phases of star formation

⋆ Based on observations made with Mopra telescope. The Mopra telescope is part of the Australia Telescope which is funded by the Commonwealth of Australia for operation as a National Facility managed by CSIRO.
⋆⋆ Table 1 and Appendix are only available in electronic form at http://www.aanda.org
⋆⋆⋆ Profiles as FITS files are only available in electronic form at the CDS via anonymous ftp to cdsarc.u-strasbg.fr (130.79.128.5) or via http://cdsweb.u-strasbg.fr/cgi-bin/qcat?J/A+A/515/A55

since dust emission is mostly optically thin and directly traces cold, high-mass dense cores on the verge of collapse, and young protostars already collapsing. Dust continuum surveys in the submm range are efficient for recognizing high-mass young stellar objects if the spatial resolution is high enough to discriminate high-mass dense cores from their surroundings. The typical size of dense cores is 0.1–0.2 parsec (e.g. Bergin & Tafalla 2007; Zinnecker & Yorke 2007), and the typical highest spatial resolution achievable on millimeter telescopes is of the order of 10″, which translates into 0.15 pc at 3 kpc. We thus propose that the massive complexes within 3 kpc offer a unique opportunity to study the earliest phases of high-mass stars.

The twin molecular complex NGC 6334-NGC 6357 (distance 1.7 kpc, size ~68 pc × ~80 pc) is one of the most prominent of these massive complexes since it includes high-mass star formation at different evolutionary stages (cores, embedded compact H II regions, evolved optical H II regions). The high-column density parts of NGC 6334-NGC 6357 were delineated using near-IR extinction maps produced from 2MASS and CO data (Schneider et al. 2010). The extinction map was derived from the publicly available 2MASS point source catalog by calculating the average reddening of stars with a method adapted from those described in Lada et al. (1994), Lombardi & Alves (2001), and Cambrésy et al. (2006). The extinction was derived from the reddening of both $[J - H]$ and $[H - K]$ colors. From the stellar population model of Robin et al. (2003), a predicted density of foreground stars was obtained at the complex distance. For each 2 arcmin size pixel of the map, this expected number of foreground stars was removed from the least reddened 2MASS sources before deriving the average reddening. Figure 1 (up) shows a global view of this complex in an Hα image from the AAO/UKST Hα survey of the southern Galactic plane (Parker et al. 2005) with the extinction map (angular resolution of 2′) superimposed. Near the H II regions, the extinction caused by dust corresponds well to the extinction zones seen in Hα (for example, the "elephant trunk" features in NGC 6334 seen at the border of the Hα extinction zone). Figure 1 (down) reproduces the 1.2 mm continuum map (angular resolution 24″) obtained by Muñoz et al. (2007), where it becomes obvious that the highest column density regions ($A_v > 30$ mag equivalent to a hydrogen column density larger than $3{\times}10^{22}$ cm^{-2}) correspond to peak emission in dust continuum. Figure 2 presents zooms at 8 μm (mosaics of GLIMPSE residual images produced by the GLIMPSE team) of NGC 6334 and NGC 6357. The 8 μm channel of the *Spitzer* IRAC instrument is dominated by PAH emission, excited by nearby ultra-violet radiation. In these images, many 1.2 mm continuum emission peaks clearly appear in the direction to IR extinction patches but only a few correspond to 8 μm emission. For the central part of NGC 6334, Burton et al. (2000) detected evidence of dark lanes parallel to the ridges and loops of 3.3 μm PAH emission. Because of the lower resolution of our extinction map, we cannot compare it directly with, but, if these dark lanes correspond well to optical extinction, only those aligned along the main ridge can be related to the 1.2 mm dust emission.

NGC 6334 is a well studied region (as reviewed by Persi & Tapia (2008). At 1.2 mm, the central part of NGC 6334 consists of a 10 pc long filament associated with large extinction. At least seven sites of high-mass star formation are observed (e.g. Loghran et al. 1986), recognizable in terms of water masers, H II regions (e.g. Carral et al. 2002), and molecular outflows. Previous (sub)millimeter continuum studies of NGC 6334 focused mainly on the northern portion of the filament containing sources I and I(N) (e.g. Sandell 2000). These sources exhibit

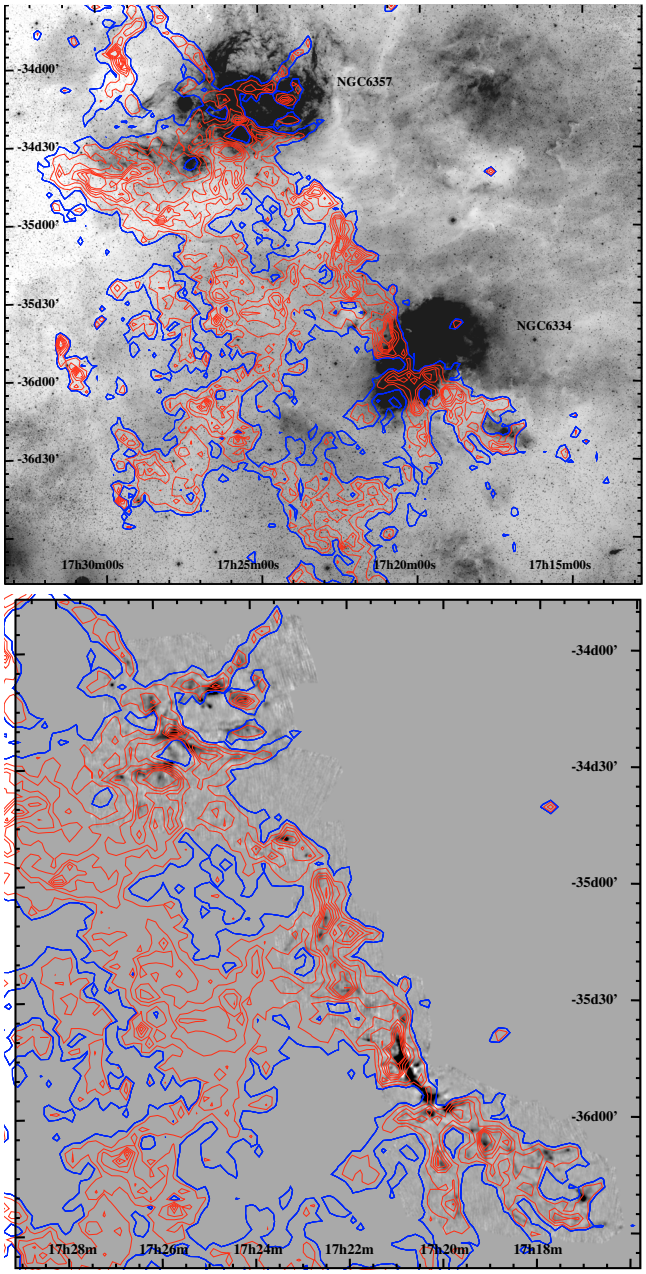

Fig. 1. *Top*: Hα image (UKST Hα survey, Parker et al. 2005) of NGC 6334 and NGC 6357 with extinction isocontours overlaid on it. Red contours correspond to A_v between 18 mag and 30 mag (by step of 2 mag) the blue contour corresponds to A_v = 16.5 mag. *Bottom*: the 1.2 mm continuum emission from Muñoz et al. (2007) with extinction isocontours overlaid.

outflows and have masses of between 200 and 400 $M_\odot$. The molecular emission associated with NGC 6334 has a mean velocity of −4 km s^{-1} with a velocity gradient (Kraemer & Jackson 1999) from the center ($V_{\rm LSR} \sim 0$ km s^{-1}) to the edge of the ridge ($V_{\rm LSR} \sim -11$ km s^{-1}). In addition to the far-IR sources, NGC 6334 is a grouping of the well-known H II regions GUM 61, GUM 62, GUM 63, and GUM 64. On the basis of the distance modulus determined by Persi & Tapia (2008), a mean distance of 1.63 ± 0.3 kpc is obtained for the exciting stars of these H II regions.

NGC 6357 is a large H II region exhibiting an annular morphology in the radio and optical (e.g. Lortet et al. 1984). Far-IR continuum data detected several luminous ($L \sim 10^5$ $L_\odot$)

embedded sources coinciding with ^{12}CO(1–0) and radio continuum emission peaks (McBreen et al. 1983). In contrast to NGC 6334, almost no water maser emission is found in NGC 6357 (Healy et al. 2004). The brightest H II region (G353.2+0.9) has a sharp boundary facing the massive open cluster Pismis 24. The distance of NGC 6357 is usually taken to be that of Pismis 24: a distance of 1.7 kpc was determined by Neckel (1978) and Lortet et al. (1984), a distance of 1.1 kpc is obtained by Conti & Vacca (1984) for a Wolf-Rayet star belonging to the cluster, and Massey et al. (2001) give a distance of 2.5 kpc.

The kinematics of NGC 6357 is around −4 km s^{-1} (ionized gas, Caswell & Haynes 1987), which is similar to the mean velocity of NGC 6334 and strongly suggests that both regions are at the same distance (1.7 kpc). In addition, the extinction map (Fig. 1) and the morphology of the 1.2 mm SIMBA emission tend to indicate that NGC 6334 and NGC 6357 are connected by a filamentary structure, thus again suggesting that both regions belong to the same complex. We therefore adopt a common distance for NGC 6334 and NGC 6357 of 1.7 kpc.

In this paper, we follow the approach of Motte et al. (2007) to characterize the star formation content of this high-mass star-forming complex and constrain the evolutionary sequence of high-mass star formation. Motte et al. (2007) applied a specific extraction method to a 1.2 mm continuum map of the Cygnus X complex to extract dense cores. They complemented these data with SiO(2–1) follow-up observations of the most likely progenitors of high-mass stars, and determined the main characteristics of the millimeter sources by searching for signposts of protostellar activity including SiO emission (a tracer of outflow activity). In Cygnus X, they identified 33 high-mass dense cores of mean size, mass, and density of 0.13 pc, 91 $M_\odot$, and 1.9×10^5 cm^{-3}, respectively. Seventeen dense cores were found to harbor high-mass protostars in their IR-quiet phase. Their unbiased survey of the high-mass young stellar objects in Cygnus X demonstrates that high-mass IR-quiet protostars do exist, and that their lifetimes should be comparable to those of more evolved high-luminosity IR protostars. By comparing the number of high-mass protostars and OB stars across the entire Cygnus X complex, a statistical lifetime of 3×10^4 yr for high-mass protostars was estimated, which is one order of magnitude smaller than the lifetime of nearby low-mass protostars, and in agreement with the free-fall time of Cygnus X dense cores.

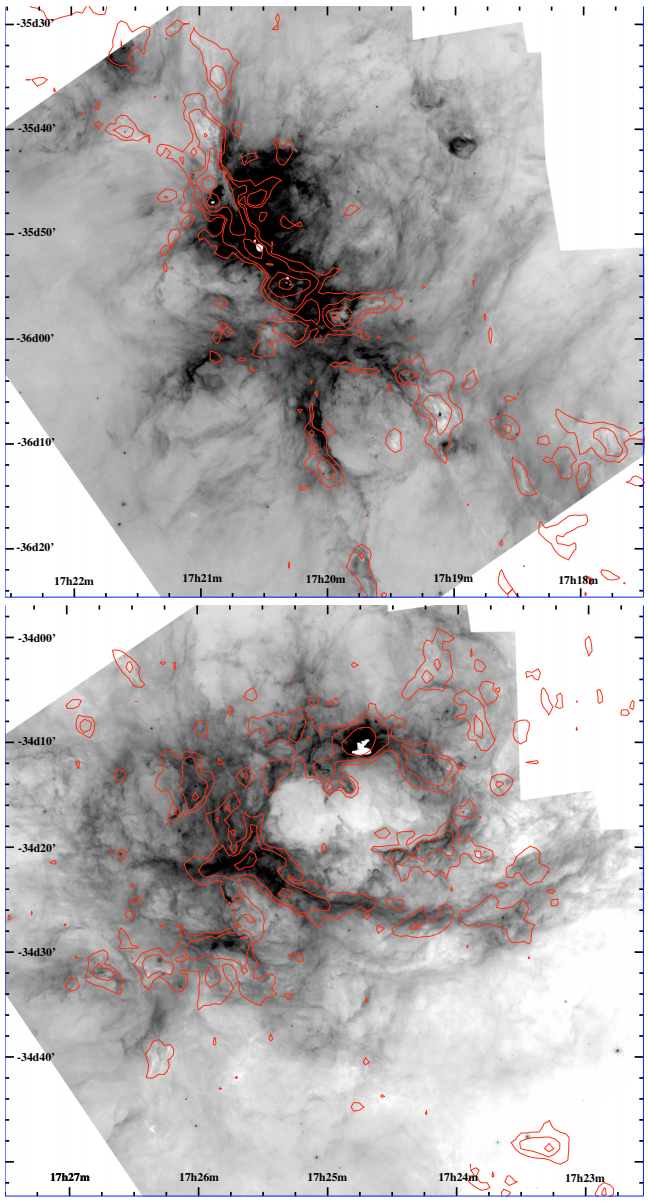

Fig. 2. GLIMPSE 8 μm residual (corrected for point sources) mosaics (produced and delivered by the GLIMPSE team) of NGC 6334 (top) and NGC 6357 (*bottom*). The 1.2 mm continuum emission isocontours are overlaid.

2. The data

2.1. Dust continuum data at 1.2 mm

The 1.2 mm (250 GHz) continuum observations of NGC 6334 and NGC 6357 and the data reduction were performed by Muñoz et al. (2007). The observations were completed using the 37-channel SEST Imaging Bolometer Array (SIMBA) in the fast-mapping mode. The angular resolution is 24″ (full width at half maximum) corresponding to a spatial resolution of 0.2 pc at 1.7 kpc. The typical pointing accuracy of the SEST telescope is 3″–5″ and SIMBA observations usually have a relative flux uncertainty of 20% (Faúndez et al. 2004). The 1.2 mm mosaic has a relatively homogeneous rms noise of ∼25 mJy beam^{-1}. The filamentary morphology of the emission becomes evident in Fig. 3. The strongest emission peaks are associated with NGC 6334 and NGC 6357. A filamentary structure, which we call "inter-region filament", is identifiable between both regions.

2.2. Molecular line observations

We performed pointed observations toward the 42 most massive dense cores ($M > 100\ M_\odot$) in the SiO ($v = 0$, $J = 2$–1) transition using the 22 m Mopra telescope. The observations were performed with the 3mm receiver and the Mopra spectrometer (MOPS) in the "zoom mode" that allows to observe simultaneously up to 16 different frequencies. The pointing was regularly checked by observing SiO masers, typical corrections required were smaller than 5″. The typical system temperature was 190 K. The velocity resolution is 0.12 km s^{-1}, the beam width at 86 GHz is 36″, and a main beam efficiency τ_{MB} of 0.49 (Ladd et al. 2005) was adopted. All observations were performed in position switching mode with the off-position a few arcminutes away. A total integrated time of 11 min on-source was used to achieve a rms of ∼0.05 K. Initial spectral processing (base-removal and calibration onto a T_A^* scale) was performed with the

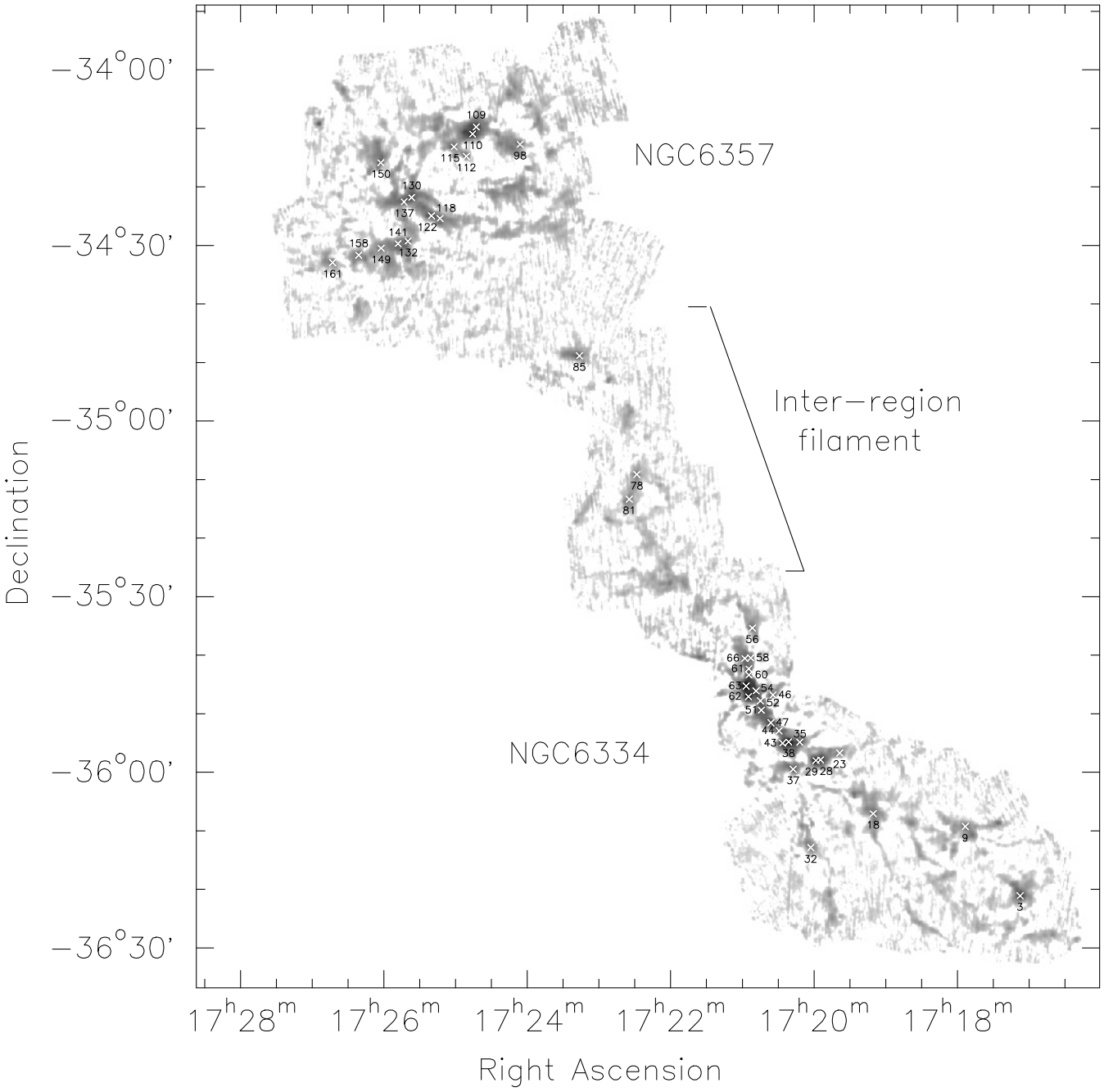

Fig. 3. Greyscale image of the 1.2 mm continuum emission toward NGC 6334 and NGC 6357 observed by Muñoz et al. (2007) with SIMBA (SEST). The white crosses indicate the 42 dense cores we have extracted that are more massive than 100 $M_{\odot}$. The core number is indicated as well, referring to the fragment number given Table 1.

ASAP software[1]. In addition to the SiO line, other molecular species (N_2H^+ (1–0), $H^{13}CO^+$ (1–0), HCN (1–0), HNC (1–0), ^{13}CS (2–1), HCO^+ (1–0), and CH_3CN (5–4)) were observed simultaneously (example spectra are presented in Fig. 4).

3. Analysis and results

3.1. The compact dense cores at 1.2 mm

Muñoz et al. (2007) identified a total of 181 clumps with sizes ranging from 0.1 to 1 pc, and a median of 0.36 pc, and masses ranging from 3 to 6000 $M_{\odot}$ with a mean value of 170 $M_{\odot}$. They extracted these clumps from NGC 6334 and the "inter-region filament" using the Clumpfind algorithm (Williams et al. 1994). Clumpfind defines a source as an emission peak that extends to a defined contour level (in Muñoz et al. 2007, 3σ = 75 mJy beam^{-1}) and separates it from other peaks/sources at saddle points located below a given level (here again 3σ) from the peaks. However, this approach is not well suited to identifying compact and dense sources and generally identifies cloud structures with a large variety of sizes, which could thus be progenitors of single stars, small groups, or even clusters of stars.

To build a more homogeneous sample of cloud fragments that would be compact enough to be called dense cores (~0.1 pc, see the terminology given in e.g. Motte et al. 2007), we use

[1] http://www.atnf.csiro.au/computing/software/

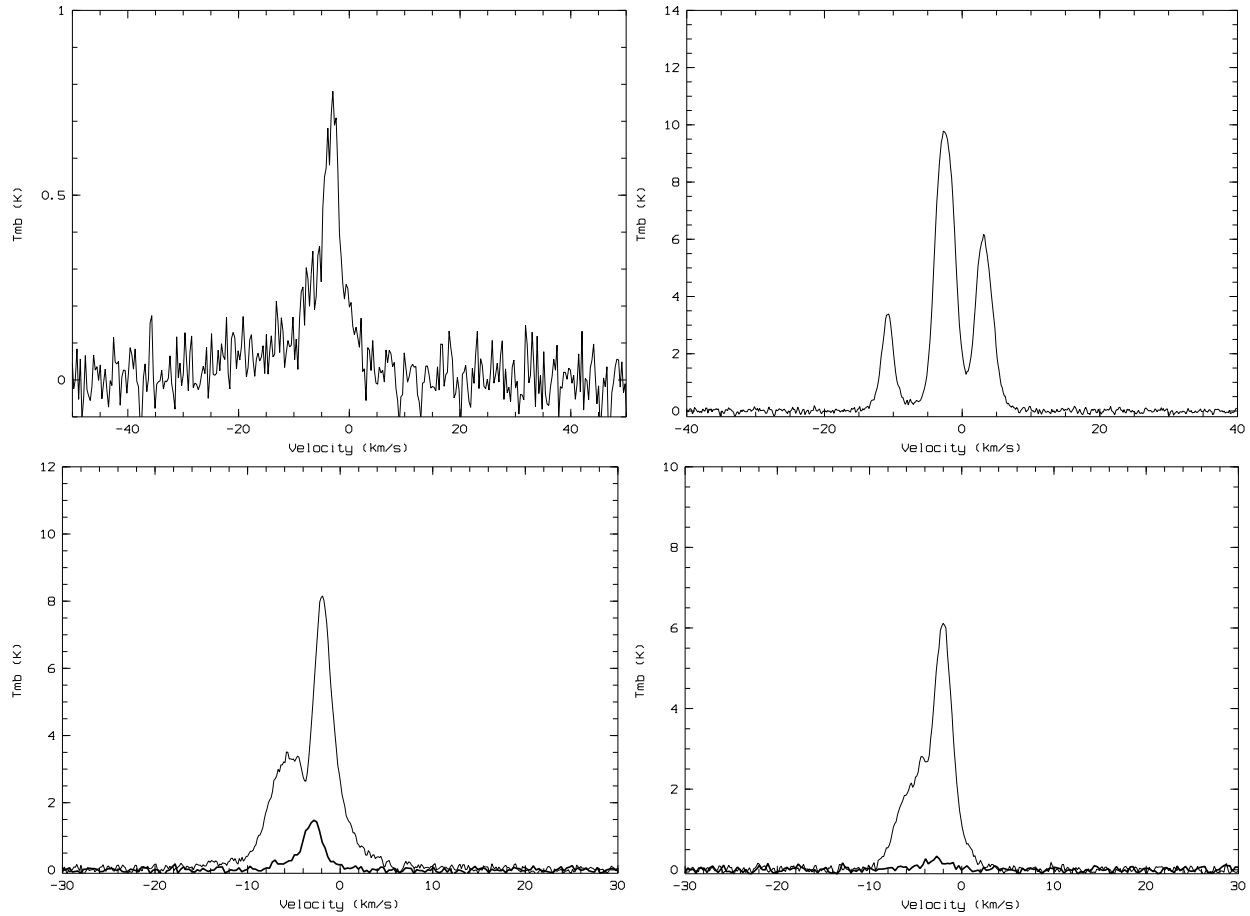

Fig. 4. Example of spectra obtained for the dense core 61 (the spectra for the other dense cores are given in the Appendix). All profiles (except for N_2H^+) have been smoothed to a velocity resolution of 0.3 km s^{-1}. *Upper panels*: SiO (*left*) and N_2H^+ (*right*). *Lower panels*: on the left HCO^+ superimposed on $H^{13}CO^+$ (thick line) and on the right HNC superimposed on ^{13}CS (thick line).

the compact source extraction method developed by Motte et al. (2003).

Our reason for excluding diffuse molecular cloud structures from our analysis is to focus on the most likely sites of current intermediate- to high-mass star formation (here called massive dense cores). The procedure described in more detail in Motte etal. (2007) uses a multi-resolution analysis (Starck & Murtagh 2006) and the Gaussclumps program (Stuzki & Gusten 1990; Kramer et al. 1998). The multi-resolution technique is based on wavelet transformations and allows us to set a cutoff length-scale that separates sources observed on different spatial scales of the 1.2 mm map. We choose to filter out spatial scales larger than 1 pc, corresponding to "clumps" according to the terminology of Williams et al. (2000) and Motte et al. (2007). The compact (≤1 pc) fragments are then identified above the 6σ (~150 mJy beam^{-1}) level in the filtered 1.2 mm map by a 2D-Gaussian fitting. As a consequence, all sources are on average compact and thus dense. We extracted 163 dense cores in total, their sizes and 1.2 mm fluxes being given in Table 1. For each core, the total mass (dust + gas) was derived by assuming that the 1.2 mm emission consists of thermal dust emission that is largely optically thin

$$M_{1.2\ \mathrm{mm}} = \frac{S^{\mathrm{int}}_{1.2\ \mathrm{mm}} d^2}{\kappa_{1.2\ \mathrm{mm}} B_{1.2\ \mathrm{mm}}(T_{\mathrm{dust}})} \quad (1)$$

where $\kappa_{1.2\ \mathrm{mm}}$ is the dust opacity per unit mass column density at 1.2 mm and $B_{1.2\ \mathrm{mm}}(T_{\mathrm{dust}})$ is the Planck function for a dust temperature T_{dust}. The dust mass opacity (including dust properties and gas-to-dust mass ratio) is likely to vary with density, temperature, and the evolutionary state of the emitting medium (Henning et al. 1995). Models of dust in low-mass protostellar cores (e.g. Ossenkopf & Henning 1994) suggest that a value of $\kappa_{1.2\ \mathrm{mm}} = 0.01$ cm^2 g^{-1} is well suited to cool (10–30 K) and high-density ($n_{H_2} \geq 10^5$ cm^{-3}) cloud fragments. We therefore choose a dust opacity per unit (gas + dust) mass column density of $\kappa_{1.2\ \mathrm{mm}} = 0.01$ cm^2 g^{-1}, although we note that this value is uncertain by a factor of 2.

The temperature to be used in Eq. (1) is the mass-weighted dust temperature of the cloud fragments, whose value could be determined from gray-body fitting of their spectral energy distributions. This measurement has been performed only for NGC 6334I(N) by Sandell (2000), who found 30 K. In addition, Matthews et al. (2008) inferred a mean temperature (derived from integrated flux density ratio 450 μm/850 μm) of ~25 K for clumps in NGC 6334. This agrees with Motte et al. (2007), who demonstrate that the temperature generally measured in dense fragments forming high-mass stars is in the range of 15–25 K. We then assume $T_{\mathrm{dust}} = 20$ K in Eq. (1). The mass estimate is correct to within a factor of 2 due to the uncertainty in the dust opacity, while an uncertainty of 30% is implied by a temperature change from 15 to 25 K.

The volume-averaged densities are then estimated to be

$$\langle n_{\mathrm{H_2}} \rangle = \frac{M_{1.2\ \mathrm{mm}}}{\frac{4\pi}{3} FWHM^3} \quad (2)$$

where $M_{1.2\ \mathrm{mm}}$ is the mass derived by Eq. (1) and *FWHM* is the geometric mean of full widths at half maximum, determined by Gaussian fits. Using a radius equal to the *FWHM* in Eq. (2), we can accurately determine the volume-averaged density because the flux (and thus the mass) measured within such an aperture corresponds to >98% of the integrated flux (respectively total mass) of Gaussian cloud structures. The often-used, beam-averaged peak density would of course be higher, but is less relevant when estimating physical constraints such as the free-fall time.

As no radio continuum data of sufficiently high resolution around 5 GHz is available, the contribution of the free-free emission from the gas to the mass calculation has been estimated from both the NVSS 1.4 GHz (beam size 45″ × 45″) image (Condon et al. 1998) and the 1.6 GHz (beam size 26″ × 20″) image (Muñoz et al. 2007). Since the 1.6 GHz image unfortunately covers only NGC 6334, we used the NVSS 1.4 GHz for NGC 6357. We then measured the radio flux in an aperture, convolved to the beam of the image, of the cores. We extrapolated this flux to 1.2 mm by assuming a power law dependence of $S_\nu \sim \nu^{-0.1}$, subtracted this flux from $S^{\mathrm{int}}_{1.2\ \mathrm{mm}}$, and recalculated the mass and density (Table 1) from the corrected value of $S^{\mathrm{int}}_{1.2\ \mathrm{mm}}$. Since the NVSS 1.4 GHz survey also covers NGC 6334, we compared the mass obtained from the 1.4 and 1.6 GHz images and found good agreement (the linear regression gives a slope of 0.95±0.0087 and constant term of 1.07±1.9), which justifies our use of the 1.4 GHz data for NGC 6357. The mass correction due to the free-free emission represents on average 6% of the $M_{1.2\ \mathrm{mm}}$. However, at 1.4 GHz and 1.6 GHz the emission is not always in the optically thin regime. This implies that our free-free correction certainly underestimates the free-free contribution at 1.2 mm and that in turn, the corrected masses are overestimated.

Table 1 summarises the properties of the extracted cores: core number (Col. 1), core coordinates (Col. 2), $S^{\mathrm{peak}}_{1.2\ \mathrm{mm}}$ (Col. 3), the deconvolved *FWHM* size (Col. 4), $S^{\mathrm{int}}_{1.2\ \mathrm{mm}}$ (Col. 5), free-free corrected mass (Col. 6) and free-free corrected density (Col. 7).

Amid the 181 clumps extracted by Muñoz et al. (2007), 68 have associations with one or several of our cores (only 11 clumps of Muñoz et al. are associated with several cores). Our cores are all found in the most massive and densest clumps of Muñoz et al. (2007): the mean mass and density of clumps with associated cores are 451 $M_\odot$ and ~1.4×10^4 cm^{-3}, respectively while for clumps without associated cores they are 50 $M_\odot$ and ~8×10^3 cm^{-3}, respectively.

3.2. Molecular lines towards high-mass 1.2 mm dense cores

N_2H^+ is a good tracer of the highest density and cold regions of clouds because it appears to be mostly optically thin and less depleted onto dust grain surfaces than CO and other molecular species (Tafalla et al. 2002, 2004, 2006). The isolated 101–012 line width of the hyperfine structure is used to estimate the virial mass and help us to quantify infall motions by comparison with optically thick lines such as HCO^+ and HNC.

The opacity and excitation temperature of the N_2H^+ 1→0 line was determined using the known hyperfine (HFS) structure pattern of this transition. The 6 relative distances and intensities of HFS components of the 1 → 0 line were given as input to a simultaneous Gaussian fit to all components, assuming equal excitation temperature. For most of the sources, one velocity component, and thus a single Gaussian HFS fit, was performed, using the "Method HFS" feature of GILDAS[2]. Few sources were found to have two velocity components and only one to have three components (core 66). However, some of the densest and most massive cores (cores 60, 61, and 63) exhibit a non-LTE HFS pattern (the relative intensities have not been correctly fitted) and rather broad linewidths. These sources probably consist of several cloud fragments along the line of sight which thus blending their N_2H^+ emission lines. In Table 2, we indicate the excitation temperature (equal for all components by definition), the line center velocity of the molecular gas bulk emission determined from the 123–013 (93.173.809 MHz) component of N_2H^+ (the receiver was tuned to this frequency), the main beam temperature, the full line width, and the opacity of the isolated 101–012 line component. The typical uncertainty estimated for these determined parameters is 15%.

Both HCO^+ and $H^{13}CO^+$ are usually used to probe the kinematics of the extended envelope and hence the bulk motion of the gas in the region. Because they are usually optically thin, ^{13}CS and $H^{13}CO^+$, are often used to establish the systemic velocity of the dense cores. All the 42 high-mass dense cores observed (Table 3) were found to have velocities in agreement with the kinematics of NGC 6334 and NGC 6357.

The asymmetric rotator CH_3CN is a good tracer of the conditions in "hot cores" owing to its favorable abundance and excitation in warm (≥100 K) and dense (≥10^5 cm^{-3}) regions. It traces objects that are internally heated and its emission is more intense and more commonly detected towards ultra-compact H II regions than towards isolated maser sources (Purcell et al. 2006). Assuming local thermal equilibrium and optically thin lines, the relative intensities of the K components yield a direct measure of the kinetic temperature (Purcell et al. 2006). Amid the 42 massive cores, 8 have well detected CH_3CN, while 13 have no detectable CH_3CN and 21 have barely detectable CH_3CN. From CH_3CN rotational diagrams, we can establish the temperature of the hot component within the 8 dense cores for which several K components of CH_3CN are observed to be: 72.5 K for core 62; 62 K for core 54; 47 K for core 60; ~42 K for cores 63, 35, and 29; 31 K for core 3; and 20 K for core 61. All these dense cores are associated with stellar activity. The temperature of the hot core inferred from CH_3CN (between 20 and 70 K) is normally higher than the dust temperature mass-averaged over 0.2 pc. This does not contradict our assumption that the mass-averaged temperature over cloud structures is 20 K on average and probably slightly higher only for the above 8 sources.

4. Origin and characteristics of high-mass dense cores

The NGC 6334 – NGC 6357 complex has already formed generations of high-mass stars since it contains OB stars and H II regions. Here we focus on its ability to form high-mass stars in the (near) future by making a census of high-mass prestellar and protostellar dense cores and comparing with the high mass star formation in Cygnus X. For Cygnus X, a lower mass limit of 40 $M_\odot$ was adopted for dense cores to have a high probability of forming 10–20 $M_\odot$ of stars, including at least one high-mass star (Motte et al. 2007). From Table 1, we note that the dense cores of NGC 6334-NGC 6357 are on average ~3 times larger than the dense cores found in Cygnus X by Motte et al. (2007). This is mainly because the physical resolution is a factor of two poorer in NGC 6334-NGC 6357 SIMBA images than

[2] Grenoble Imaging and Line Data Analysis software

Table 2. Fitted parameters for the isolated N_2H^+ 101–012 line component using the "method HFS" from the GILDAS software

Core number	Comp. number	V_{lsr} (km s^{-1})	τ	*FWHM* (km s^{-1})	T_{mb} (K)	T_{ex} (K)
3	1	−3.85	0.04	1.37	0.01	4.1
9	1	−9.43	0.09	2.34	0.54	9.3
	2	−2.72	1.93	1.34	0.14	2.9
18	1	−4.34	0.03	1.96	0.69	26.3
23	1	−5.49	0.49	1.13	1.40	6.6
28	1	−7.35	0.11	1.64	1.20	14.3
	2	−5.05	0.01	1.74	0.84	79.8
29	1	−5.71	0.01	2.84	1.21	113.6
32	1	−2.15	0.54	1.20	0.15	3.1
35	1	−4.72	0.13	1.45	1.66	16.6
37	1	−4.74	0.01	2.22	1.31	122.6
38	1	−1.62	0.08	1.87	0.87	13.9
	2	−4.06	0.14	1.68	0.25	4.8
43	1	1.25	0.06	1.96	0.65	13.9
	2	−1.21	0.01	1.97	0.24	25.5
44	1	−1.93	0.15	1.39	0.76	8.5
46	1	−5.59	0.10	1.62	0.42	7.4
47	1	−1.23	0.04	1.54	0.54	14.7
51	1	−2.78	0.01	3.29	0.12	14.2
52	1	−1.29	2.28	2.35	0.22	3.0
	2	−2.00	0.02	4.00	0.34	16.7
54	1	−9.44	0.07	2.36	0.53	10.9
	2	−2.68	0.88	1.51	0.12	2.9
56	1	−3.18	0.37	1.57	1.12	6.6
58	1	−2.67	6.62	2.29	1.72	30.0
60	1	−3.85	0.01	4.32	1.76	163.2
61	1	−2.70	0.01	3.33	1.76	163.2
62	1	−7.33	0.01	3.95	1.36	126.7
	2	−10.0	0.05	19.4	0.01	4.5
63	1	−4.56	0.13	4.09	2.49	22.8
	2	−4.55	0.16	4.05	0.82	8.6
66	1	−0.92	0.27	3.78	0.67	5.8
	2	−3.17	0.01	1.85	0.88	82.8
	3	−6.17	0.18	0.50	0.59	6.6
78	1	0.86	0.29	5.38	0.12	3.3
	2	−3.89	0.05	1.65	0.22	7.1
81	1	2.28	0.14	1.70	0.79	9.1
85	1	−2.09	0.05	2.43	0.80	19.2
98	1	−4.28	0.01	2.21	0.16	18.3
109	1	−3.87	0.01	1.45	0.01	8.0
110	1	−5.60	0.53	1.23	0.18	3.2
112	1	−8.43	0.26	1.80	0.53	5.3
115	1	−5.19	0.12	1.25	0.18	4.5
118	1	−2.04	0.01	1.67	0.34	34.3
	2	−4.65	0.02	1.66	0.75	37.5
122	1	−3.83	0.07	1.91	0.35	7.7
130	–	–	–	–	–	–
132	1	−3.03	0.04	1.56	0.62	17.0
137	–	–	–	–	–	–
141	1	−0.29	0.02	2.48	0.13	9.1
	2	−3.60	0.06	1.86	0.14	5.3
149	1	−3.11	0.01	1.53	0.56	54.1
150	1	−4.16	0.11	1.80	0.17	4.4
158	1	−2.34	9.48	2.01	0.34	6.9
	2	1.52	0.24	1.92	0.18	3.7
161	1	−1.76	0.01	2.03	0.24	25.0

in Cygnus X MAMBO2 ones, which needs to be taken into account when adopting a low-mass limit. If we assume[3] that the cores have a $\rho(r) \propto r^{-2}$ density gradient, for high-mass stars to be formed with a similar probability, the lower mass limit for the fragments extracted in NGC 6334-NGC 6357 needs to be ~3 times higher than the Cygnus X one. We therefore choose a lower mass limit of 100 $M_\odot$ to select a sample of high-mass dense cores that are expected to be good candidate progenitors of high-mass stars.

The 42 compact cloud fragments identified in NGC 6334-NGC 6357 with masses higher than 100 $M_\odot$ have sizes ranging from 0.16 to 0.63 pc with a mean size of ~0.36 pc (see Table 1) and mean volume-averaged density of $\sim 7 \times 10^4$ cm^{-3}. After correcting for the free-free contamination, the mass range of our sample is between 101 $M_\odot$ and 1951 $M_\odot$. The cloud structures extracted in NGC 6334-NGC 6357 are thus slightly smaller in size and 10 times denser than typical HMPOs (high-mass protostellar objects, Beuther et al. 2002) and IRDC (infrared dark cloud, Rathborne et al. 2006) clumps (HMPOs and IRDCs have typical sizes of 0.5 pc and their respective typical mass and density are 290 $M_\odot$ and 150 $M_\odot$ and 8.5×10^3 cm^{-3} and 5.9×10^3 cm^{-3}; see Table 4 of Motte et al. 2007). Therefore, the NGC 6334 - NGC 6357 dense cores are on average, more likely host precursors of high-mass stars.

4.1. Correlation of 1.2 mm dense cores with signposts of stellar activity

To determine the origin of the massive cores detected at 1.2 mm, we studied their spatial association with the following signposts of stellar activity.

4.1.1. Association with *Spitzer*/GLIMPSE

The position of sources in the [3.6]–[4.5] versus [5.8]–[8] diagram is related to the presence of circumstellar dust. The principal classification scheme for low-mass star formation is the class 0-I-II-III system, which notably characterizes objects in terms of their IR excesses or SEDs (e.g. Adams et al. 1987; André et al. 1993, 2000). Class 0 and I objects are understood to be protostars surrounded by dusty infalling envelopes, which would explain both the relatively strong far-IR emission and significant near-IR extinction from their envelopes. They are deeply embedded objects with a spectral energy distribution (SED) that peaks in the submillimeter or the far-IR, indicating that the source of emission is cold dust. Class II systems are optically visible stars with disks, and thus exhibit a smaller IR excess and near-IR extinction (unless observed edge-on). Class III objects are essentially stars without significant amounts of circumstellar dust.

To establish an association of dense cores with class I and class II objects (see Table A.1), we used the IRAC/GLIMPSE point source catalogue (http://irsa.ipac.caltech.edu/data/SPITZER/GLIMPSE/). The class is defined using [5.8]–[8.0] and [3.6]–[4.5] colors and based on models of disk or envelopes or both, Allen et al. (2004) defined the criteria:

class I: [5.8]–[8.0] ≥ 0.35 and [3.6]–[4.5] > 0.4,
class II: [5.8]–[8.0] ≥ 0.35 and [3.6]–[4.5] ≤ 0.4.

The distribution of class II sources in the [3.6]-[4.5] color diagram depends mainly on the accretion rate, while the disk inclination and the grain properties explain the spread in the [5.8]–[8.0] color. The larger distribution spread in both colors, [3.6]–[4.5] and [5.8]–[8.0], for class I objects is due to the higher temperature and density of the envelope. However, an extinction of

[3] The mass limit will be considerably higher in the case of cores with a flatter density profile.

Table 3. Turbulence support, SiO outflow, and gravitational infall of the most massive dense cores of NGC 6334 - NGC 6357.

Core number	M_{vir} ($M_\odot$)	f_{turb}	V_{lsr} (km s^{-1})	T_{SiO} (K)	$FWHM_{SiO}$ (km s^{-1})	$\Delta v_{outflow}$ (km s^{-1})	$\int T_{sio} dv$ (K km s^{-1})	δV HCO$^+$	δV HNC	T_B/T_R HCO$^+$	T_B/T_R HNC	Possible nature
3	120	2.51	−10.77	0.23	2.8	7.00	0.35 ± 0.08	−5.01	−5.23	–	–	CH II region
9	160	2.46	−9.46	0.42	5.8	23.2	2.3 ± 0.09	−5.52	−5.23	–	4.17	IR-Quiet protostar
18	328	3.60	−4.19	–	–	–	–	−0.54	−0.39	3.87	2.64	IR-Quiet protostar
23	139	2.07	−5.36	–	–	–	–	−0.27	−0.53	–	–	starless core
28	168	3.02	−6.03	–	–	–	–	1.48	1.48	–	0.90	starless core
29	461	5.24	−5.94	0.30	6.2	17.8	1.4 ± 0.09	0.17	0.21	–	–	IR-Bright protostar
32	166	2.20	−2.36	–	–	–	–	0.32	0.16	0.16	–	starless core
35	142	2.67	−4.77	0.29	5.4	10.3	0.8 ± 0.09	0.20	0.07	–	–	IR-Quiet protostar
37	424	4.08	−5.09	0.29	6.6	11.8	1.2 ± 0.09	−0.03	0.05	–	–	IR-Quiet protostar
38	195	3.08	−2.48	0.44	4.9	13.9	1.8 ± 0.10	0.61	0.96	–	–	CH II region
43	216	3.62	+0.07	0.30	3.9	9.1	0.99 ± 0.09	−1.03*	−0.93	–	–	IR-Quiet protostar
44	164	2.55	−2.11	0.16	3.3	6.0	0.55 ± 0.09	−0.23	−0.23	–	–	IR-Quiet protostar
46	168	2.97	−5.11	–	–	–	–	−0.02	0.04	–	10.17	starless core
47	215	2.82	−0.83	0.13	0.3	9.9	0.57 ± 0.08	0.11	0.04	–	–	CH II region
51	1446	6.07	−3.54	0.15	5.7	11.3	0.82 ± 0.09	0.30	−0.83	0.89	1.08	CH II region
52	691	7.39	−2.35	0.10	5.9	8.4	0.59 ± 0.07	−0.10	−0.21	–	0.17	IR-Quiet protostar
54	85	2.76	−4.15	0.13	10.7	17.3	1.3 ± 0.08	−2.13*	−2.06	–	–	IR-Quiet protostar
56	205	2.88	−3.40	–	–	–	–	0.34	0.65	0.37	0.88	starless core
58	391	4.22	−4.35	–	–	–	–	0.18*	0.05	0.44	0.29	starless core
60	332	5.36	−3.98	1.08	5.8	23.2	7.0 ± 0.29	−0.62	−0.52	1.70	1.56	IR-Quiet protostar
61	326	3.93	−2.97	0.78	4.5	29.0	4.8 ± 0.15	0.44	0.39	0.40	0.46	IR-Quiet protostar
62	525	7.29	−7.06	0.57	6.0	24.1	3.8 ± 0.14	−0.21	−0.18	6.10	9.93	UCH II region
63	997	7.54	−4.77	2.41	6.6	66.3	25.4 ± 0.40	−0.35	−0.13	2.94	–	IR-Quiet protostar
66	300	3.41	−6.29	–	–	–	–	0.01*	0.01	0.69	0.60	starless core
78	216	3.04	−4.11	–	–	–	–	−0.20*	−0.20	3.50	3.98	starless core
81	234	3.12	+1.93	–	–	–	–	0.29	0.29	–	–	starless core
85	295	4.47	−2.50	0.16	–	13.1	0.84 ± 0.07	−0.59	−0.06	8.87	–	HCH II region?
98	328	4.06	−4.14	–	–	–	–	−0.19	−0.06	–	–	IR-Quiet protostar
109	253	2.66	−3.35	–	–	–	–	0.09	0.02	0.34	0.25	CH II region
110	130	2.26	−5.90	–	–	–	–	−0.24	−0.16	–	–	CH II region
112	194	3.31	−8.48	0.007	4.2	6.2	0.30 ± 0.06	−0.07	0.09	–	–	IR-Quiet protostar
115	92	2.28	−5.47	–	–	–	–	−0.17	−0.09	1.06	0.75	starless core
118	313	3.05	−3.28	0.10	–	3.6	0.17 ± 0.08	−0.04*	−0.04	2.12	1.24	IR-Quiet protostar
122	286	3.53	−3.88	0.067	–	4.7	0.38 ± 0.07	−0.10	0.05	0.09	–	IR-Quiet protostar
130	–	–	−7.52	–	–	–	–	–	–	0.31	0.36	CH II region
132	155	2.88	−3.18	–	–	–	–	−0.01	−0.07	–	–	starless core
137	–	–	−6.87	–	–	–	–	–*	–	1.05	0.77	starless core
141	359	3.43	−2.76	–	–	–	–	−0.28	−0.18	–	1.81	IR-Quiet protostar
149	193	2.81	−3.43	–	–	–	–	0.17	0.24	0.13	–	starless core
150	136	3.32	−4.68	0.0086	0.97	2.2	0.10 ± 0.06	−0.30	−0.14	–	–	IR-Quiet protostar
158	438	3.70	−1.74	–	–	–	–	−0.35*	−0.15	2.18	2.49	starless core
161	276	3.75	−1.98	–	–	–	–	−0.09	0.00	4.93	–	starless core

Notes. Column 1: the core number as in Table 1 (numbers in boldface indicate the $M > 200\ M_\odot$ cores). Column 2: the virial mass (see Sect. 4.2.2). Column 3: the internal turbulence (see Sect. 4.2.1). Column 4: the systemic velocity deduced from ^{13}CS and/or H^{13}CO$^+$. Columns 5 to 8: the peak line intensity, the line width at half maximum, full line width at the base and integrated intensity of the SiO emission. Columns 9 to 12 (see Sect. 4.2.4): the asymetric parameter and the blue to red peak ratio of the HCO$^+$ and HNC lines. Asterisk in the δV_{HCO^+} column indicates dense cores suspected to have several components present along the line of sight. Column 13: the possible nature of the source: Compact H II region (CH II region), ultra-compact H II region (UCH II region), hyper-compact H II region (HCH II region), IR-quiet protostar, IR-bright protostar, or starless core.

30 mag causes a shift of about 0.4 mag toward redder [3.6]-[4.5] indices, implying that class II sources can fall in the class I area. Based on the mean extinction found for the dense cores (estimated from the extinction map), we can consider a source as a true class I, if its [3.6]-[4.5] color is above 0.8. Hartmann et al. (2005) confirm the criteria of Allen et al. (2004) on the basis of observations of the Taurus pre-main sequence stars.

We establish a physical association with *Spitzer*/GLIMPSE point sources when the *Spitzer*/GLIMPSE point source(s) fall within 6″ (i.e. upper limit to the sum of the maximum pointing error 5″ and the typical GLIMPSE position accuracy 0.3″) of the dense core center. This is justified because high-mass protostars are expected to form at the center of the dense core. In this way, only 10 dense cores have such an association. They are all associated with true class I objects except core 152, which is associated with a class II object.

The *Spitzer*/GLIMPSE point sources sample may be contaminated by galaxies. Chavarria et al. (2008) established a criterion to separate young stellar objects from galaxies, which is roughly that [4.5]< 14.5. Assuming that it can be applied to NGC 6334-NGC 6357, all of the *Spitzer*/GLIMPSE point sources associated

Table 4. High-mass young stellar objects in NGC 6334-NGC 6357 ($M > 200\ M_\odot$) compared to Cygnus X cores and HMPOs clumps.

	Cygnus X	NGC 6334 - NGC 6357	HMPOs
SiO	93%	80%	?
Size (pc)	0.13	0.37	0.5
Mass ($M_\odot$)	91	617	290
$\langle n_{H_2} \rangle$ (cm^{-3})	1.7×10^5	1.5×10^5	8.5×10^3

with the dense massive cores have [4.5] between 6.21 and 11.44 and are thus most probably young stellar objects.

4.1.2. Association with radio sources and masers

We used the SIMBAD database[4] to look for additional signposts of stellar activity provided by centimeter free-free emission and OH, H_2O, and CH_3OH masers. We define an association when the object is located within the *FWHM* size of the core.

An association with a source of free-free emission was established by using the 1.4 GHz SGPS survey (Haverkorn et al. 2006) and the 843 MHz MOST survey (Green et al. 1999), which were both correlated with the NVSS catalog given by Condon et al. (1998) and with White (2005) catalog. We cannot check the nature of the detected cm-emission with the current database, but it is probably caused by the emission of H II regions. Since a systematic search for masers in the area studied here does not exist, we checked the dense core association with known masers in the literature. We found a correlation with maser emission for 8 sources (e.g. Pestalozzi et al. 2005, Caswell et al. 2008, Moran et al. 1980; Caswell & Phillips 2008; Val'tts et al. 1999), 3 of which are also radio sources. The systemic velocity of the associated maser(s) is in good agreement with the general kinematics of NGC 6334-6357, except for core 163 (methanol and H_2O masers, $V_{LSR} = -50$ km s^{-1}). Either these masers are caused by an outflow or core 163 is not associated with NGC 6334 - 6357.

4.1.3. Association with 24 μm sources

Correlation with mid-IR sources was determined by using *MSX*-21 μm, and *Spitzer*/MIPSGAL-24 μm (Carey et al. 2009) data. For *MSX* we used the point-source catalogue (Egan et al. 1999), while for *Spitzer*/MIPSGAL we used aperture photometry from the post-basic calibrated data available at IPAC server[5]. As high-mass protostars are expected to form at the center of the dense core and because little *Spitzer*/MIPSGAL 24 μm or *MSX*-21 μm emission can be extended, we define a physical association when the source falls within the delimitation of the core but not farther than 23″ from the dense core center. This value is adopted on the basis of the association of core 51 with *MSX* 21 μm extended emission for which association is morphologicaly clear, while the *MSX* point-source catalogue position is at 23″ from the SIMBA peak.

The 24 μm flux was measured using SAOImage DS9 with "funtools", through both a 6.5″ and 13″ circular aperture (depending on the source size). The background correction is estimated from a 7″–13″, 20–30″, or 40–50″ annulus, depending on the background structure and crowding. An aperture correction is applied depending on the size of the background annulus (Engelbracht et al. 2007). The typical uncertainty in the aperture measurement deduced from the "funtools" errors is 2%. Since the uncertainty in the MIPS flux is, however, dominated by the background, we estimated a typical uncertainty of 20% from different local background measurements. Owing to the sensitivity of the MIPSGAL survey, the brightest areas are saturated. For cores in these areas, we adopted the *MSX*-21 μm flux. To scale these fluxes to the 24 μm, fluxes we measured the 24 μm flux of about 20 known *MSX*-21 μm sources and derived the best-fit linear regression (slope = 1.13 constant term=−0.64). Assuming that the relation is applicable to both high fluxes and the spectral distribution of our objects, we then multiplied all 21 μm flux by 1.13. In this way, 51 dense cores have a 24 μm flux (see Table A.1).

For a large sample of red sources, Robitaille et al. (2008) show that young stellar objects and AGB stars can generally be separated using simple color-magnitude criteria, sources with [4.5]>7.8 and [8.0]–[24.0] ≥ 2.5 probably being young stellar objects. All cores associated with *Spitzer*/GLIMPSE and 24 μm fluxes (2 cores have *Spitzer*/GLIMPSE but no *Spitzer*/MIPSGAL detection and thus cannot be classified) follow these criteria and are probably young stellar objects. The other cores with 24 μm flux detections should only be labeled as having a high probability of being young objects since contamination by planetary nebulae or background galaxies represents at most 3% of all red sources (Robitaille et al. 2008).

4.1.4. High-luminosity and infrared-quiet cores

Dense cores that are luminous at IR wavelengths are usually considered to be good high-mass protostars or UCH II candidates (e.g. Wood & Churchwell 1989). Following Motte et al. (2007), we qualify as "high-luminosity IR sources" those dense cores of bolometric luminosity higher than $10^3\ L_\odot$, which corresponds to that of a B3 star on the main sequence. This luminosity converts into a MIPS 24 μm flux of ∼15 Jy, this flux being estimated in the same way as described in Motte et al. (2007), assuming that the luminosity of high-mass protostars is dominated by their mid- to far-IR luminosity and that their average colors are as defined by Wood & Churchwell (1989, see their Table 1). Following this definition, we have 11 high-luminosity and high mass ($M > 100\ M_\odot$) dense cores, 9 of which are associated with star formation activity (Fig. 5). In contrast, only 3 out of 30 high mass IR-quiet dense cores exhibit stellar activity. These 27 high-mass IR-quiet dense cores are probably high-mass prestellar dense cores.

4.2. Turbulence level and kinematics

From molecular lines we investigate here the turbulence level and the kinematics (virial mass, infall, outflow) of the high-mass cores.

4.2.1. Turbulence

The width of emission lines in star-forming clouds are indicative the gravitational boundness of a molecular region. According to Goldsmith (1987), sites of high-mass star formation are characterized by large line widths. In contrast, dark clouds which are isolated sites of low-mass star formation, have considerably smaller line widths. Caselli et al. (2002) derived typical line widths of 0.33 km s^{-1} for clumps in which no *IRAS* source is detected. In our sample the line widths of the N_2H^+ isolated line vary from 1.13 to 5.38 km s^{-1} (see Table 1) and are thus

[4] http://simbad.u-strasbg.fr/simbad/
[5] http://irsa.ipac.caltech.edu/applications/Spitzer/Spitzer

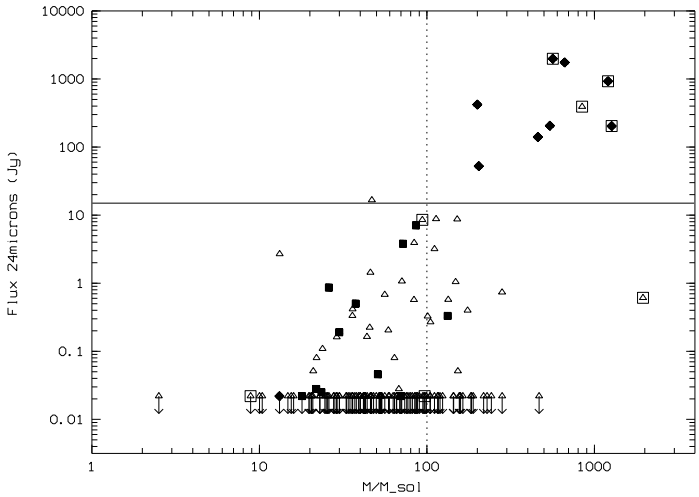

Fig. 5. Separating the high-luminosity sources from IR-quiet dense cores on the basis of their 24 μm flux (limit set to 15 Jy). The dense cores (open triangles) can be associated with masers (open squares), class I/II sources (filled squares), or radio sources (black diamonds)

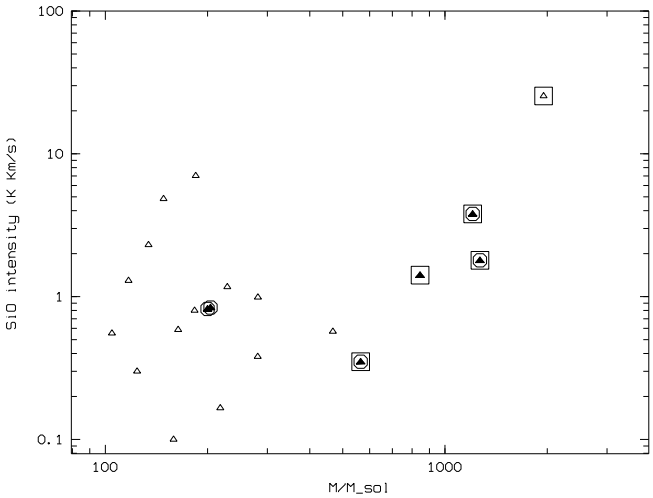

Fig. 6. Integrated intensity of SiO (2-1) detected toward the dense cores with $M_{1.2\ \mathrm{mm}} > 100\ M_\odot$ as a function of their mass. The symbols are: IR-quiet souces (open triangles), H II region (open circles), maser association (open squares), high-luminosity dense core (filled triangles).

much larger than those in the Caselli et al. (2002) study. In addition, the N_2H^+ line width is much higher than the thermal width (0.62 km s^{-1} for $T = 20$ K), emphasizing the importance of turbulence and other non-thermal motions such as outflow, infall, and rotation. However the relative contributions of these systematic motions to the line width appear to be small compared to the turbulent component (Mardones et al. 1997). Following Kirk et al. (2007), we calculate the non-thermal component σ_{NT} of the velocity dispersion from the width of the isolated N_2H^+ line and derive the level of internal turbulence f_{turb} defined by Kirk et al. (2007) to be the ratio of σ_{NT} to the mean thermal velocity dispersion of the gas (sound speed of 0.23 km s^{-1}). We note that all cores have $f_{\mathrm{turb}} > 1$ and that on average f_{turb} is slightly larger for NGC 6334 ($\langle f_{\mathrm{turb}}\rangle = 4.15 \pm 1.72$) than for NGC 6357 ($\langle f_{\mathrm{turb}}\rangle = 3.15 \pm 0.56$).

4.2.2. The virial mass

For the 42 high-mass dense cores, the virial mass was calculated to be (e.g. Walsh et al. 2007)

$$M_{\mathrm{vir}}(M_\odot) = 210\, R\langle\delta v\rangle^2 \quad (3)$$

where R is the core radius (in pc) and δv is the linewidth of the isolated line of the N_2H^+ hyperfine structure component in km s^{-1}. We assume that the velocity dispersion measured in the pointed observations represents the value that would be present across the entire core, as demonstrated to be the case by e.g. Kirk et al. (2007). This expression is valid for homogeneous, spherically symmetric objects with no external pressure and no magnetic field. If the density of the cores were to decrease outwards, the virial mass should be multiplied by $\frac{3}{5}\frac{(5-2p)}{(3-p)}$, where p is the power law index of the density radial profile. For $p \sim 2$ (Motte & André 2001; Shirley et al. 2002), this factor is ~0.6 implying that the calculated virial masses are upper limits. The virial mass is the minimum mass required for a cloud to be gravitationally bound, i.e. $\frac{M}{M_{\mathrm{vir}}} > 0.5$. (e.g. Pound & Blitz 1993). However, since the submillimeter masses are uncertain by a factor of 2 and the virial masses are upper limits, Motte et al. (2003) estimated that the $\frac{M}{M_{\mathrm{vir}}}$ ratio must be larger than 0.2 for gravitational boundness. In this case, only core 51 is not gravitationally bounded.

4.2.3. SiO outflow

The next step is to establish the proto-stellar status on the basis of the SiO outflow detection. From Table 3, we note that the SiO outflow intensity and velocity are similar to that detected in Cygnus X and for a large sample of high-mass objects (Harju et al. 1998). The detection rates are 67% for NGC 6334 and 25% for NGC 6357. The global detection rate is thus 49% (58% and 47% for high-luminosity and IR-quiet objects, respectively), clearly different from the Cygnus X value of 93%. This is probably not caused by different instrumental sensitivities because we designed our SiO observations to reach similar detection limits as the observation performed for Cygnus X. In addition, the faintest Cygnus X SiO peak intensity detected is above the faintest SiO detection of our sample. For a sample of H_2O and OH masers sources and ultracompact H II regions, Harju et al. (1998) measured a detection rate that decreases with Galactocentric distance and increases with FIR luminosity. They found a rate of 58% for Galactocentric distances of between 6 and 8 kpc (the Galactocentric distance of NGC 6334 - NGC 6357 is ~6.83 kpc) in agreement with our value.

On average, we also note that the high-luminosity and IR-quiet dense cores with SiO outflows are, respectively, 15 and 4 times denser than those without a SiO outflow. We can estimate that the typical density that a core should have to ensure an SiO outflow is $\sim 6.5 \times 10^4$ cm^{-3}. This may explain why the detection rate is higher in Cygnus X, because the Cygnus X dense cores are on average less massive but denser ($\langle n_{H_2}\rangle = 1.1 \times 10^5$ cm^{-3}) than the NGC 6334 - NGC 6357 dense cores ($\langle n_{H_2}\rangle = 2.7 \times 10^4$ cm^{-3}). Finally, in contrast to Motte et al. (2007) the high-mass IR-quiet dense cores are not found to clearly exhibit brighter SiO emission than IR-bright dense cores.

4.2.4. Infall motions

To complete our census of high-mass prestellar and protostellar dense cores, we now search for signposts of infall motions. Infall motions can be studied by investigating the profiles of optically thick molecular lines (here we use HCO^+ and HNC) that have a blue asymmetric structure, i.e. a double peak with a brighter blue peak, or a skewed single blue peak (e.g.

Myers et al. 1996; Mardones et al. 1997). To exclude the possibility that the profile is caused by two velocity components along the line of sight, an optically thin line needs to peak close to the velocity of the self-absorption dip of the optically thick line (e.g. Zhou et al. 2003; Choi et al. 1995; Wu & Evans 2003). By examining the line profiles of the optically thin $H^{13}CO^+$ line, we identified dense cores with these multiple emitting regions along the line of sight and find that most of them are composed of a single broad line with a self-absorption dip. The optically thick HNC and HCO^+ lines (see Appendix B), however, often show non-Gaussian, broad lines that are caused by several clumps along the line-of-sight and/or bulk motions of the envelope gas (e.g. cores 9, 28, 35, 37, 52) and outflow emission (e.g. cores 35, 37, 46, 52, 54). This is expected since the beam of around 40″ is rather large. To extract more distinctive infall profiles, higher angular resolution is required. However, as a first order approximation, we can still quantify the blue asymmetry of a line by using the asymmetry parameter δV defined by Mardones et al. (1997) $\delta V = \frac{V(\mathrm{thick})-V(\mathrm{thin})}{\mathrm{d}V(\mathrm{thin})}$. This is the difference between the peak velocities of an optically thick line V(thick) and an optically thin line $V(thin)$ in units of the optically thin line full width at half-maximum ($FWHM$) d$V(thin)$. We adopt the criterion of Mardones et al. (1997) for blue ($\delta V < -0.25$) and red asymmetry ($\delta V > 0.25$). We assume HNC and HCO^+ to be optically thick lines and the isolated component of the N_2H^+ hyperfine structure to be the optically thin line used to determine δV (see Table 3).

Another approach to characterizing infall motion in double-peak spectra is to measure the ratio of the blue to red peak (Wu & Evans 2003). A "blue profile" fulfills the criterion $\frac{T_B}{T_R} > 1$. The results are given in Table 3 and line asymmetry measured from HCO^+ and HNC are presented in Fig. 7.

We now have four criteria to quantify infall and establish that infall has been detected when two of them are fulfilled. In this way, apart from the cores already associated with outflow emission and those suspected to be due to two components along the line of sight, only cores 18 and 23 have a high probability of exclusively exhibiting infall motions. The core 18 – due to its 24 μm counterpart and its infall motion – has a high probability of being proto-stellar in nature. For core 23, on the basis of only infall motion, no clear decision can be made about its proto-stellar nature.

5. Lifetime and massive star formation in NGC 6334 – NGC 6357

Table 3 summarizes the characteristics of the most massive denses cores ($M > 100\ M_\odot$). The cores 62 and 63 were classified as a UCH II region and IR-quiet protostar, respectively, because they are, respectively, the well studied regions NGC 6334I and NGC 6334I(N), and we can compare with the literature. This agrees with the results of Walsh et al. (2010) and Thorwirth et al. (2003), who provide evidence, on the basis of a multi-line (around 3 mm) analysis, that NGC 6334I appears more evolved than NGC 6334I(N).

Since our sample is complete for embedded high-mass young stellar objects, we can statistically estimate the *relative lifetime* of high-mass IR-quiet and high-luminosity protostars as well as prestellar sources. To achieve this, we assume a constant star-formation rate over the past 1–2 Myr, which is justifiable because the complex exhibits sources at all stages of evolution distributed not too far apart from each other within the cloud. The lifetime estimated here is close to that found by the study in

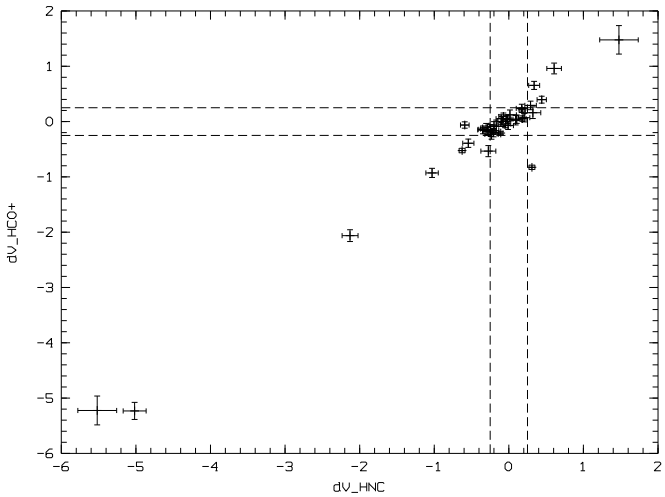

Fig. 7. Comparison of the measured asymetry in HCO^+ and HNC. The dashed lines mark $|\ \delta V\ | = 0.25$. δV < -0.25 indicates blue asymmetry while δV > 0.25 indicates red asymmetry.

Cygnus X for which no burst of star formation had been quantitatively established (Motte et al. 2007). We also need to estimate the content of massive stars (earlier than B3) in NGC 6334 and NGC 6357, since the statistical lifetime is measured relative to the known age of OB stars. *Absolute lifetimes* of the different high-mass phases may also be estimated from their free-fall dynamical timescale.

In NGC 6357, two open clusters are referenced in the literature, the well known Pismis 24 and AH03J1726-34.4 (Dias et al. 2002). For Pismis 24, Wang et al. (2008) identified from X-ray studies 34 O-B3 stars, while Damke et al. (2006) estimate a density of 40 stars per arcmin^2 for AH03J1726-34.4 (size 2.6 arcmin), i.e., approximately 200 stars for this cluster leading to about 60 O-B3 stars.

For NGC 6334, Neckel (1978) found 14 O-B3 stars from optical photometry and Bica et al. (2003) listed 7 embedded clusters/groups associated with radio sources. Tapia et al. (1996) estimated that the clusters towards NGC 6334I and NGC 6334E contain 93 and 12 O-B3 stars, respectively. In parallel, Bochum 13, a cluster at the north-west border of NGC 6334 contains 5 O-B3 stars (McSwain 2005), and UBV data from a field comprising NGC 6334, NGC 6357 and the inter-region filament provide an estimate of 40 O-B3 stars (Russeil et al. in preparation). We thus estimate 300 massive stars (earlier than B3) for the entire complex.

For Cygnus X and its total of 120 O stars, the expected number of massive stars (earlier than B3) can be inferred to be 660 using the mass function slope obtained and both the spectral type and mass conversion used in Knödlseder (2000).

From Fig. 5, we note that most of the cores with radio and/or maser counterparts have $M > 200\ M_\odot$. For Cygnus X, observed with a 0.09 pc resolution, the mass selection of $M > 40\ M_\odot$ allowed us to select dense cores with high-mass star activity (H II region, strong infrared counterpart, masers, or strong SiO outflow). This difference can be explained by our lower spatial resolution than the observations for Cygnus X, which implies we select less dense cores than in Cygnus X. In the case of NGC 6334 - NGC 6357, the average density (2.4×10^4 cm^{-3}, while the average density is 1.4×10^5 cm^{-3} for $M > 200\ M_\odot$ cores) and the weak stellar activity found towards starless $100\ M_\odot < M < 200\ M_\odot$ cores suggest they are probably forming intermediate- to low-mass stars. A large part of the IR-quiet massive cores with

mass between 100 and 200 $M_\odot$ may therefore harbor low-mass to intermediate-mass protostars that are not detected here, while others could be low-mass to intermediate-mass pre-stellar cores. This result indirectly shows that starless clumps probably have density profiles flatter than r^{-2} and confirms that resolutions of 0.1 pc are necessary to focus on sites of high-mass star formation. After selecting cores with $M > 200\ M_\odot$, the number of high-mass progenitors is 16 (6 IR-quiet massive cores, 9 high-luminosity protostars, 1 starless clump). In addition, this new mass selection brings the SiO detection rate of the NGC 6334-NGC 6357 massive dense cores yet closer to that of Cygnus X (80% versus 93%, see Table 4).

Table 5 summarizes the number, characteristics, and lifetimes of our massive dense core sample ($M > 200\ M_\odot$) at each evolutionary stage and compares them to those found in Cygnus X and nearby low-mass star-forming regions. Following the definition of Motte et al. (2007), a starless clump is defined as a high-mass core without any indication of stellar activity, an IR-quiet high-mass protostar is a high-mass core with stellar activity (H II region, masers, or SiO outflow) but 24 μm flux lower than 15 Jy (see Sect. 4.1.4), and a high-luminosity IR core is a high-mass core with stellar activity and a 24 μm flux higher than 15 Jy. Table 4 compares the characteristics of the high-mass protostellar dense cores (IR-quiet and high-luminosity IR protostellar cores) of NGC 6334-NGC 6357 to those in Cygnus X and to HMPOs. In both tables, values given for Cygnus X and HMPOs are taken from Motte et al. (2007).

On average, the size of the cores in NGC 6334-NGC 6357 are similar whatever the evolutionary stage of the core, while the mean mass, hence the mean density, increases from starless clumps to high-luminosity cores. This is consistent with the material of dense cores concentrating itself towards its center during the star formation process.

Evans et al. (2009) find median lifetimes of 4.6×10^5 yr, 1.6×10^5 yr, and 5.4×10^5 yr, respectively, for low-mass pre-stellar cores, class 0, and class I stars. However, substantial variation in lifetime estimates from cloud to cloud are observed. For example, Wilking et al. (1989) in Ophiuchus and Kenyon et al. (1990) in the Taurus-Auriga region measure for class I sources a lifetime of 2–4 $\times 10^5$ yr and 1.2×10^5 yr respectively. In Ophiuchus, André & Montmerle (1994) obtain 5×10^3–1×10^4 yr for class 0 and 10^5 yr for class I. In this framework, the NGC 6334-NGC 6357 protostellar phase lifetime (1.5×10^5 yr) is similar to the typical lifetime of nearby low-mass class 0 sources, but younger than that of class I stars. This suggests high-mass stellar formation proceeds more rapidly than for low-mass stars.

A high-mass pre-stellar core can be defined as a starless clump with a size of ~0.1 pc and a volume-averaged density of $\sim 10^5$ cm^{-3}, which is gravitationally bound (Motte et al. 2007). In Cygnus X, no such pre-stellar dense core was found. For NGC 6334-NGC 6357, the low spatial resolution of our data has prevented us from detecting these pre-stellar dense cores. We detect only one starless clump with a mean size of 0.29 pc and a mean density of 4.1×10^4 cm^{-3}, which is smaller and denser than those found in Cygnus X (~0.8 pc size and $\sim 7 \times 10^3$ cm^{-3} density). That we have detected only one starless core agrees with Hatchell & Fuller (2008). They show that the ratio of protostellar cores to starless cores increases with mass, there being ultimately no starless cores at all at the highest masses (above 12 $M_\odot$). They suggest that this implies that either more massive cores have relatively short pre-stellar lifetimes or the masses may continue to increase well into the protostellar phase. The absence of high-mass pre-stellar cores and their short lifetimes ($\leq 10^3$ yr) are discussed by Motte et al. (2007), who suggest that high-mass pre-stellar cores are dynamically evolving into protostars.

In addition, the statistical lifetime of the starless clump is shorter than the estimated free-fall time. It is also shorter than the lifetimes observed in nearby regions that form mostly low-mass stars, since starless cloud structures with volume-averaged densities of $\sim 10^3$ cm^{-3} and $\sim 10^4$ cm^{-3} have pre-stellar lifetimes of $\sim 10^6$ yr and $\sim 10^5$ yr (see Fig. 11 of Kirk et al. 2007, and references therein). Therefore, high-mass pre-stellar cores seem to be short-lived or even transient features compared to both nearby low-mass pre-stellar cores and high-mass protostars. This suggests that a supersonic dynamical process should be acting to create pre-stellar condensations from starless clumps. Short lifetimes are theoretically expected in molecular clouds, where high levels of turbulence dominate and pre-stellar cores are magnetically supercritical (e.g. Vásquez-Semadeni et al. 2005), in agreement with the turbulence levels observed within these cores. These dynamical processes are also necessary for the protostellar lifetime to last for only one free-fall time and, consequently, for the accretion to be strong enough ($\sim 10^{-3}\ M_\odot$ yr^{-1}) to overcome the radiation pressure and form a high-mass star.

When comparing protostellar cores in NGC 6334 and NGC 6357, we note that they have different mean densities ($\sim 1.7 \times 10^4$ cm^{-3} and $\sim 1.9 \times 10^5$ cm^{-3} for NGC 6357 and NGC 6334, respectively), which suggests that an environmental and/or external process is needed to explain this difference.

The comparison of the NGC 6334 – NGC 6357 and Cygnus X proto-stellar cores (Tables 4 and 5) show that both regions have similar cores densities and similar protostellar phase timescales, while the mass and size of NGC 6334 – NGC 6357 cores are higher and larger than those of Cygnus X. In addition to the lower SiO detection rate,this implies that the cores in NGC 6334 - NGC 6357 are statistically more evolved than those in Cygnus X.

6. Conclusions

To improve our knowledge of high-mass star formation, Motte et al. (2007), by studying Cygnus X, started an unbiased study of its earliest phases, i.e. the high-mass analog of low-mass pre-stellar cores and class 0 protostars. We have applied the same strategy to the star-forming complex NGC 6334 – NGC 6357. We have performed SiO(2-1) follow-up observations of 42 high-mass dense cores ($\geq 100\ M_\odot$), the most likely progenitors of intermediate-mass to high-mass stars, detected in a 1.2 mm continuum map.

Our results can be summarized as follows:

1. We have used the *MSX*-21 μm and *Spitzer*/MIPSGAL-24 μm fluxes of our 1.2 mm high-mass dense cores to identify high-luminosity ($>10^3\ L_\odot$) high-mass young stellar objects. More than half of the dense cores are considered to be good candidate precursors of high-mass stars and are found to be IR-quiet (i.e. 33 dense cores more massive than 100 $M_\odot$ have $F_{24\ \mu\mathrm{m}} < 15$ Jy).
2. We have surveyed our sample of high-mass ($\geq 100\ M_\odot$) dense cores in SiO(2-1) to search for shocked gas in molecular outflows and/or hot cores. In contrast to Cygnus X, we do not find any association of high-velocity SiO emission with all high-mass IR-quiet cores. In this way, 15 cores have been classified as starless clumps.

Table 5. High-mass young objects in NGC 6334 - NGC 6357 ($M > 200\ M_\odot$) at various stages of the high-mass star formation process.

	Starless clumps	High-mass IR-quiet protostars	High-luminosity IR protostars	O-B3 stars
NGC 6334 – NGC 6357				
Number	1	6	9	300
$\langle size \rangle$	0.29 pc	0.38 pc	0.37 pc	
Statistical lifetime[1]	$\sim 1 \times 10^4$ yr	$\sim 6 \times 10^4$ yr	$\sim 9 \times 10^4$ yr	$\sim 3 \times 10^6$ yr
$\langle M \rangle$	242 $M_\odot$	571 $M_\odot$	664 $M_\odot$	
$\langle n_{H_2} \rangle$	4.1×10^4 cm^{-3}	1.1×10^5 cm^{-3}	1.9×10^5 cm^{-3}	
Free-fall time[2]	4.9×10^4 yr	8×10^4 yr		
Cygnus X				
Number[3]	10	17	25	660
Statistical lifetime	3×10^4 yr	$\sim 5.1 \times 10^4$ yr	$\sim 7.6 \times 10^4$ yr	$(2 \pm 1) \times 10^6$ yr
Free-fall time	4×10^5 yr	8×10^4 yr		
Statistical lifetime in dark clouds	2×10^5 yr	2×10^4 yr	2×10^5 yr	

Notes. [(1)] Lifetime calculated relative to the known age of the stars in the young cluster Pismis 24 (cf. Massey et al. 2001 and Ahumada et al. 2007) using the census given in line 1. [(2)] Free-fall time measured from the mean values of the volume-averaged density given line 5: $t_{\rm free-fall} = \sqrt{\frac{3\pi}{32G\langle\rho\rangle}}$ [(3)] The numbers of OB3 stars in Cygnus X and thus the statistical lifetimes of high-mass young stellar objects have been corrected from the values given in Motte et al. (2007).

3. A $M \geq 200\ M_\odot$ selection appears more appropriate for selecting cores with high-mass star activity in NGC 6334 - NGC 6357, while for Cygnus X the selection for smaller dense cores was $M \geq 40\ M_\odot$.
4. Our unbiased survey of the high-mass young stellar objects ($M \geq 200\ M_\odot$) confirms the results of the previous study of Cygnus X: high-mass IR-quiet protostars do exist and their lifetime is comparable to that of more evolved high-luminosity IR protostars. We have estimated the statistical lifetime of high-mass protostars to be 1.8×10^5 yr, similar to the statistical lifetime (1.3×10^5 yr) of high-mass protostars in Cygnus X.
5. Only one starless clump is observed, suggesting that starless clumps rapidly concentrate and collapse to form high-mass protostars. The starless clump that we observe is smaller, denser and less massive (~0.3 pc, $\sim 4 \times 10^4$ cm^{-3}, 242 $M_\odot$) than those of Cygnus X (~0.8 pc, $\sim 7 \times 10^3$ cm^{-3}, 800 $M_\odot$).
6. Lifetime measurements of the pre-stellar and protostellar IR-quiet phases of high-mass stars in NGC 6334 - NGC 6357 infer that a dynamical process is regulating their evolution. Highly turbulent processes throughout the molecular cloud complex would be necessary in such a dynamical picture of the high-mass star formation process.

To observe the high-mass star formation process during its earliest phases, far-IR to sub-millimeter continuum imaging of the entire NGC 6334 - NGC 6357 star-forming complex (such as that proposed with *Herschel* by Motte, Zavagno, Bontemps et al.: the HOBYS Key Programme) will be very useful. In particular, the 75/110/170 μm PACS and 250/350/500 μm SPIRE images of the HOBYS project will provide an unbiased census of both massive pre-stellar cores and massive Class 0-like protostars, and will trace the large-scale emission surrounding the cores. For the first time, this will provide accurate far-infrared photometry, which is essential for deriving good luminosity and mass estimates (from spectral energy distributions) of our high-mass dense cores sample. In addition, high angular resolution molecular line data will be required to trace in more detail the infall and outflow signatures of the protostellar sources.

Acknowledgements. The authors thanks the PNPS for financial support for the Mopra Observations. This paper is part of the ANR PROBES scientific framework. The Mopra telescope is part of the Australia Telescope which is funded by the Commonwealth of Australia for operation as a National Facility managed by CSIRO. The University of New South Wales Digital Filter Bank used for the observations with the Mopra Telescope was provided with support from the Australian Research Council. This research has made use of the SIMBAD database, operated at CDS, Strasbourg, France. A large Part of this work was done thanks to *Spitzer* (GLIMPSE and MIPSGAL) data.

References

Ahumada, A., Clariá, J., & Bica, E. 2007, A&A, 473, 437
Adams, F., Lada, C., & Shu, F. 1987, ApJ, 312, 788
Allen, L., Calvet, N., D'alessio, P., et al. 2004, ApJS, 154, 363
André, P., & Montmerle, T. 1994, ApJ, 420, 837
André, P., Ward-Thompspn, D., & Barsony, M. 1993 ApJ, 406, 122
André, P., Ward-Thompspn, D., & Barsony, M. 2000, in Protostars and Planets IV, ed. V. Mannings, A. P. Boss, & S. Russel (Tucson: Univ. Arizona Press), 59
Ballesteros-Paderes, J., Gazol, A., & Kim, J. et al. 2006, ApJ, 637, 384
Bergin, E., & Tafalla, M. 2007, ARAA, 45, 339
Beuther, H., & Schilke, P. 2004, Sci, 303,1167
Beuther, H., Schilke, P., Menten, K., et al. 2002, ApJ, 566, 945
Bica, E., Dutra, C., & Barbuy, B. 2003, A&A, 397, 177
Bonnell, I., & Bate, M. 2002, MNRAS, 336, 659
Bonnell, I., & Bate, M. 2006, MNRAS, 370, 488
Burton, M., Ashley, M., Marks, R., et al. 2000, ApJ, 542, 359
Cambrésy, L., Beichman, C. A., & Jarrett, T. H., 2002, AJ, 123, 2559
Caselli, P., Benson, P., Lyers, P., et al. 2002, ApJ, 572, 238
Caswell, J., & Haynes, R. 1983, AuJPh, 36, 361
Caswell, J., & Haynes, R. 1987, A&A, 171, 261
Caswell, J., & Phillips, C. 2008, MNRAS, 386, 1521
Caswell, J., Batchelor, R., Forster, J., et al. 1983, AuJPh, 36, 401
Carey, S., Noriega-Crespo, A., Mizuno, D., et al. 2009, PASP, 121, 76
Carral, P., Kurtz, S., & Rodríguez, L. 2002, AJ, 123, 2574
Chavarria, L., Allen, L., Hora, J., et al. 2008, ApJ, 682, 445
Choi, M., Evans, N., Gregersen, N., et al. 1995, ApJ, 448, 742
Condon, J., Cotton, W., Greisen, E., et al. 1998, AJ, 115, 1693
Conti, P., & Vacca, W. 1990, AJ, 100, 431
Damke, G., Barba, R., & Morrell, N. 2006, Rev. Mex. Astron. Astrofis., 26, 180
Dias, W., Alessi, B., Moitinho, A., et al. 2002, A&A, 389, 871
Egan M. P., et al. 1999, The Midcourse Space Experiment Point Source Catalog, Version 1.2, Explanatory Guide (AFRL-VS-TR-1999-1522). Natl. Tech. Inf. Serv., Springfield, VA
Engelbracht, C., Blaylock, M., Su, K., et al. 2007, PASP, 119, 994
Evans, N., Dunham, M., Jorgensen, J., et al. 2009, ApJS, 181, 321
Faúndez, S., Bronfman, L., Garay, R., et al. 2004, A&A, 426, 97

Goldsmith, P., Snell, R., & Hasegawa, T. 1987, ApJ, 314, 525
Green, A., Cram, L., Large, M., et al. 1999, ApJS, 122, 207
Hanson, M. 2003, ApJ, 597, 957
Harju, J., Lehtinen, K., Booth, R., et al. 1998, A&ASS, 132, 211
Hartmann, L., Megeath, S., Allen, L., et al. 2005, ApJ, 629, 881
Hatchell, J., & Fuller, G. 2008, A&A, 482, 855
Hatchell, J., Fuller, G., Richer J., et al. 2007, A&A, 468, 1009
Haverkorn, M., Gaensler, B., McClure-Griffiths, N., et al. 2006, ApJS, 167, 230
Healy, K., Hester, J., & Claussen, M. 2004, ApJ, 610, 835
Heitsch, F., Hartmann, L., Slyz, A., et al. 2008, ApJ, 674, 316
Henning, T., Michel, B., & Stognienko, R. 1995, P&SS, 43, 1333
Kirk, H., Johnstone, D., & Tafalla, M. 2007, ApJ, 668, 1042
Kenyon, S., Hartmann, L., Strom, K., et al. 1990, AJ, 99, 869
Kerton, C., Martin, P., Johnstone, D., et al. 2001, ApJ, 552, 601
knödlseder, J. 2000, A&A, 360, 539
Koenig, X., Allen, L., Gutermuth, R., et al. 2008, ApJ, 688, 1142
Kraemer, K., & Jackson, J. 1999, ApJS, 124, 439
Kramer, C., Stutzki, J., & Rohrig, R. 1998, A&A, 329, 249
Lada, C. J., Lada, E. A., Clemens, D. P., et al. 1994, ApJ, 429, 694
Ladd, N., Purcell, C., Wong, T., et al. 2005, PASA, 22, 62
Lombardi, M., & Alves, J. 2001, A&A, 377, 1023
Lortet, M., Testor, G., & Niemela, V. 1984, A&A, 140, 24
Loughran, L., McBreen, B., Fazio, G., et al. 1986, ApJ, 303, 629
Mardones, M., Myers, P., Tafalla, M., et al. 1997, ApJ, 489, 733
Martin-Pintado, J., Bachiller, R., & Fuente, A. 1992, A&A, 254, 315
Massey, P., DeGioia-Eastwood, K., & Waterhouse, E. 2001, AJ, 121, 1050
Matthews, H., McCutcheon, W., Kirk, H., et al. 2008, AJ, 136, 2101
McBreen, B., Jaffe, D., & Fazio, G. 1983, AJ, 88, 835
McKee, C., & Tan, J. 2002, Nature, 416, 59
McSwain, M., & Gies, D. 2005 ApJS, 161, 118
Motte, F., & André P. 2002, A&A, 365, 440
Motte, F., André, P., & Neri, R. 1998, A&A, 336, 150
Motte, F., Schilke, P., & Lis, D. 2003, ApJ, 582, 277
Motte, F., Bontemps, S., Schilke, P., et al. 2007, A&A, 476, 1243
Moran, J., & Rodriguez, L. 1980, ApJ, 236, L159
Muñoz, D., Mardones, D., Garay, G., et al. 2007, ApJ, 668, 906
Myers, P. C., Mardones, D., Tafalla, M., Williams, J. P., & Wilner, D. J. 1996, ApJ, 465, L133
Neckel, T. 1978, A&A, 69, 51
Ossenkopf, V., & Henning, T. 1994, A&A, 291, 943
Parker, Q., Phillipps, S., Pierce, M., et al. 2005, MNRAS, 362, 689
Pestalozzi, M., Minier, V., & Booth, R. 2005, A&A, 432, 737
Peretto, N., Hennebelle, P., & André, P. 2007, A&A, 464, 983
Persi, P., & Tapia, M. 2008, Handbook of Star Forming Regions, Vol.II: The Southern Sky ASP Monograph Publications, ed. Bo Reipurth, 5, 456
Pound, M., & Blitz, L. 1993, ApJ, 418, 328
Purcell, C., Balasubramanyam, R., Burton, M., et al. 2006, MNRAS, 367, 553
Rathborne, J., Jackson, J., & Simon, R. 2006, ApJ, 641, 389
Robitaille, T., Meade, M., Babler, B., et al. 2008, AJ, 136, 2413
Robin, A., Reylé, C., Derrière, S., et al. 2003, A&A, 409, 523
Sandell, G. 2000, A&A, 358, 242
Schneider, N., Bontemps, S., Simon, R., et al. 2010, A&A, submitted [arXiv:1001.2453]
Shirley, Y., Evans, N., & Rawlings, J. 2002, ApJ, 575, 337
Starck, J., & Mutargh, F. 2006 Astronomical image and data analysis, Astronomy and Astrophysics Library (Berlin: Springer)
Stutzki, J., & Guesten, R. 1990, ApJ, 356, 513
Tafalla, M., Myers, P., Caselli, P., et al. 2002, ApJ, 569, 815
Tafalla, M., Myers, P., Caselli, P., et al. 2004, A&A, 416, 191
Tafalla, M., Santiago-Garcia, J., Myers, P., et al. 2006, A&A, 455, 577
Tapia, M., Persi, P., & Roth, M. 1996, A&A, 316, 102
Thorwirth, S., Winnewisser, G., Megeath, S., et al. 2003, ASP Conf. Ser., 287, 257
Val'tts, I., Ellingsen, S., & Slysh, V. 1999, MNRAS, 310, 1077
Vásquez-Semadeni, E., Kim, J., Shadmehri, J., et al. 2005, ApJ, 618, 344
Walborn, N., Howarth, I., Lennon, D., et al. 2002, AJ, 123, 2754
Walsh, A., Myers, P., Di Francesco, J., et al. 2007, ApJ, 655, 958
Walsh, A., Thorwirth, S., Beuther, H., et al. 2010, MNRAS, 404, 1396
Wang, J., Townsley, L., Feigelson, E., et al. 2007, ApJS, 168, 100
Wilking, B., Lada, C., & Young, E. 1989, ApJ, 340, 823
Williams, J., de Geus, E., & Blitz, L. 1994, ApJ, 428, 693
Williams, S., Blitz, S., & McKee, C. 2000, in Protostars & Planets IV, ed. Mannings, V., et al. (Tucson: Univ. Arizona Press), 97
White, R., Becker, R., & Helfand, D. 2005, AJ, 130, 586
Wood, D., & Churchwell, E. 1989 ApJS, 69, 831
Wu, J., & Evans, N. 2003, ApJ, 592, L79
Zhou, S., Evans, N., Kompe, C., et al. 1993, ApJ, 404, 232
Zinnecker, H., & Yorke, H. 2007 ARA&A, 45, 481

Pages 15 to 18 are available in the electronic edition of the journal at http://www.aanda.org

Table 1. Properties of dense cores detected in NGC 6334-NGC 6357.

Core number	Core name	$S^{\rm peak}_{1.2\ {\rm mm}}$ (mJy/beam)	*FWHM* (pc×pc)	$S^{\rm int}_{1.2\ {\rm mm}}$ (mJy)	M ($M_\odot$)	$\langle n_{\rm H_2}\rangle$ (cm^{-3})
1	J171613.6-362835	180	0.31×0.22	480	25	6.1×10^3
2	J171633.5-362739	240	0.31×0.27	760	39	6.7×10^3
3	J171701.8-362106	3400	0.32×0.29	11500	564	8.2×10^4
4	J171705.1-361957	290	0.26×0.06	480	24	5.6×10^4
5	J171707.8-361906	320	0.46×0.19	1120	59	9.4×10^3
6	J171711.0-362639	180	0.37×0.31	690	36	3.9×10^3
7	J171721.6-360842	550	0.31×0.17	1360	72	2.4×10^4
8	J171743.4-361040	400	0.40×0.29	1590	84	8.9×10^3
9	J171749.2-360916	450	0.52×0.34	2540	134	7.6×10^3
10	J171759.0-361323	240	0.32×0.23	690	36	7.8×10^3
11	J171826.7-361415	170	0.49×0.23	710	38	4.1×10^3
12	J171827.1-362545	170	0.50×0.14	570	30	6.5×10^3
13	J171828.7-361250	160	0.71×0.17	800	42	4.2×10^3
14	J171835.0-360841	300	0.50×0.36	1670	88	4.8×10^3
15	J171905.1-360638	170	0.43×0.12	450	24	9.1×10^3
16	J171906.2-360821	250	0.50×0.24	1080	53	5.3×10^3
17	J171906.3-361039	200	0.60×0.19	870	45	4.9×10^3
18	J171907.4-360704	530	0.57×0.29	2860	151	9.3×10^3
19	J171913.0-360613	180	0.26×0.26	490	23	5.6×10^3
20	J171919.2-360327	160	0.52×0.19	620	33	4.3×10^3
21	J171923.6-360342	500	0.38×0.27	1820	96	1.2×10^4
22	J171928.6-360958	180	0.58×0.25	900	36	2.6×10^3
23	J171936.3-355642	270	0.82×0.32	2220	116	3.6×10^3
24	J171941.0-362453	200	0.49×0.31	1010	53	3.6×10^3
25	J171943.3-362046	270	0.40×0.24	970	52	7.0×10^3
26	J171944.2-355617	210	0.28×0.15	440	23	1.2×10^4
27	J171950.8-355715	170	0.06×0.06	170	3	5.5×10^4
28	J171952.5-355752	1540	0.32×0.27	4890	242	4.1×10^4
29	J171956.3-355758	5520	0.32×0.23	16290	844	1.7×10^5
30	J171957.9-355740	240	0.06×0.06	240	9	1.9×10^5
31	J171958.7-360846	160	0.31×0.11	350	15	1.0×10^4
32	J171959.9-361252	320	0.80×0.37	2790	144	3.8×10^3
33	J172002.8-361158	220	0.37×0.28	810	43	5.3×10^3
34	J172007.5-360908	290	0.40×0.22	980	52	8.0×10^3
35	J172010.0-355452	940	0.44×0.23	3540	183	2.3×10^4
36	J172012.8-355857	310	0.38×0.22	980	52	9.1×10^3
37	J172015.4-355928	830	0.41×0.41	4360	228	1.3×10^4
38	J172019.5-355449	7050	0.45×0.24	27220	1267	1.4×10^5
39	J172019.6-354229	160	0.28×0.17	370	13	5.4×10^3
40	J172021.5-355848	270	0.41×0.27	1030	53	5.9×10^3
41	J172023.4-355253	320	0.30×0.06	610	23	3.6×10^4
42	J172023.5-355532	240	0.06×0.06	240	10	2.0×10^5
43	J172024.6-355502	1870	0.32×0.22	5360	281	6.2×10^4
44	J172027.7-355255	470	0.65×0.25	2650	105	6.4×10^3
45	J172031.1-360104	200	0.44×0.28	820	44	4.3×10^3
46	J172033.1-354648	730	0.42×0.22	2580	113	1.6×10^4
47	J172034.6-355132	1760	0.62×0.30	10400	467	2.4×10^4
48	J172036.8-354948	230	0.37×0.09	540	10	7.4×10^3
49	J172040.2-354903	210	0.32×0.06	390	–	–
50	J172040.9-355042	230	0.28×0.25	640	25	5.5×10^3
51	J172042.7-354923	820	0.67×0.60	9180	200	3.2×10^3
52	J172043.6-354747	880	0.70×0.06	3280	163	8.4×10^4
53	J172045.7-355004	170	0.24×0.17	350	–	–
54	J172047.3-354605	780	0.53×0.06	2230	117	9.1×10^4
55	J172049.5-354458	570	0.27×0.06	960	50	1.0×10^5
56	J172050.9-353521	580	0.49×0.32	2930	153	1.0×10^4

Table 1. continued.

Core number	Core name	$S^{\rm peak}_{1.2\ {\rm mm}}$ (mJy/beam)	*FWHM* (pc×pc)	$S^{\rm int}_{1.2\ {\rm mm}}$ (mJy)	M ($M_\odot$)	$\langle n_{H_2} \rangle$ (cm^{-3})
57	J172051.8-353431	170	0.42×0.31	740	37	3.2×10^3
58	J172052.0-354028	450	0.48×0.26	1980	105	9.7×10^3
59	J172052.6-354414	440	0.22×0.06	670	36	9.9×10^4
60	J172053.6-354322	1530	0.35×0.10	3500	184	1.1×10^5
61	J172053.6-354219	720	0.37×0.31	2820	148	1.5×10^4
62	J172053.7-354703	13910	0.17×0.15	22980	1206	1.2×10^6
63	J172055.7-354516	11910	0.31×0.26	36860	1951	3.5×10^5
64	J172056.1-354135	350	0.29×0.11	710	37	2.7×10^4
65	J172056.8-353933	270	0.39×0.20	860	46	8.7×10^3
66	J172057.0-354032	660	0.45×0.38	3580	189	1.0×10^4
67	J172102.0-353130	210	0.31×0.15	500	26	1.1×10^4
68	J172102.9-353850	210	0.51×0.30	1020	54	3.8×10^3
69	J172108.1-354306	230	0.40×0.14	630	33	1.0×10^4
70	J172111.6-355007	190	0.30×0.26	570	29	5.6×10^3
71	J172116.4-354634	270	0.51×0.27	1250	66	5.3×10^3
72	J172135.0-354023	650	0.34×0.15	1620	86	3.1×10^4
73	J172136.5-353152	150	0.57×0.22	700	26	2.3×10^3
74	J172140.4-354011	180	0.38×0.06	380	20	2.6×10^4
75	J172147.3-352756	220	0.66×0.32	1430	76	3.2×10^3
76	J172200.4-352741	340	0.34×0.24	1060	56	1.0×10^4
77	J172203.5-352447	150	0.64×0.22	760	40	3.1×10^3
78	J172228.5-350908	420	0.40×0.35	1910	101	8.1×10^3
79	J172230.8-351117	170	0.36×0.24	550	29	4.8×10^3
80	J172233.8-345828	180	0.49×0.28	830	44	3.6×10^3
81	J172234.7-351321	430	0.53×0.28	2110	111	8.0×10^3
82	J172237.8-351347	180	0.27×0.15	390	21	9.9×10^3
83	J172252.3-351650	210	0.43×0.22	740	39	5.9×10^3
84	J172251.9-345304	370	0.33×0.17	960	51	1.5×10^4
85	J172316.6-344851	1540	0.27×0.21	3850	204	5.9×10^4
86	J172318.9-351709	150	0.32×0.20	410	22	5.4×10^3
87	J172320.7-344845	420	0.30×0.25	1200	64	1.3×10^4
88	J172326.2-344831	270	0.43×0.27	1110	59	6.0×10^3
89	J172329.0-344841	230	0.30×0.26	670	36	6.8×10^3
90	J172340.9-341412	270	0.56×0.34	1620	84	4.0×10^3
91	J172350.6-342101	280	0.42×0.36	1350	71	5.1×10^3
92	J172350.6-340838	290	0.61×0.20	1320	70	6.7×10^3
93	J172352.8-340929	170	0.27×0.06	300	16	3.1×10^4
94	J172357.7-340606	190	0.28×0.22	490	26	7.3×10^3
95	J172358.8-341653	260	0.47×0.14	810	42	1.0×10^4
96	J172404.0-342051	240	0.25×0.21	550	29	1.0×10^4
97	J172404.1-341909	200	0.66×0.32	1320	70	3.0×10^3
98	J172406.0-341243	700	0.32×0.32	2510	133	1.7×10^4
99	J172410.3-341958	250	0.66×0.25	1390	74	4.5×10^3
100	J172410.1-340248	180	0.71×0.17	880	47	4.4×10^3
101	J172412.1-341325	320	0.50×0.28	1510	80	6.3×10^3
102	J172414.6-340414	300	0.38×0.32	1220	64	6.4×10^3
103	J172416.6-342007	220	0.49×0.18	780	42	6.6×10^3
104	J172420.5-342802	190	0.64×0.54	1880	99	2.0×10^3
105	J172421.7-341242	230	0.33×0.33	860	46	5.5×10^3
106	J172424.3-341103	270	0.40×0.16	760	40	1.1×10^4
107	J172427.2-342152	170	0.23×0.23	400	21	6.9×10^3
108	J172427.8-342102	300	0.41×0.41	1600	85	5.2×10^3
109	J172442.3-340945	1260	0.68×0.48	11650	459	1.0×10^4
110	J172445.3-341058	3120	0.49×0.33	16200	665	4.2×10^4
111	J172446.1-340933	440	0.23×0.06	690	13	3.6×10^4
112	J172450.5-341446	750	0.37×0.22	2350	124	2.3×10^4

Table 1. continued.

Core number	Core name	$S^{peak}_{1.2\ mm}$ (mJy/beam)	*FWHM* (pc×pc)	$S^{int}_{1.2\ mm}$ (mJy)	M ($M_\odot$)	$\langle n_{H_2} \rangle$ (cm^{-3})
113	J172451.1-341042	1110	0.23×0.22	2560	94	3.4×10^4
114	J172459.2-341449	270	0.27×0.20	650	34	1.1×10^4
115	J172500.6-341309	760	0.33×0.24	2310	119	2.2×10^4
116	J172502.8-342550	210	0.64×0.31	1300	68	3.2×10^3
117	J172503.6-341312	230	0.19×0.15	410	20	1.7×10^4
118	J172512.4-342523	480	0.71×0.41	4120	218	5.8×10^3
119	J172512.9-342617	270	0.23×0.18	580	30	1.5×10^4
120	J172512.1-340824	240	0.45×0.34	1190	63	4.3×10^3
121	J172515.0-341003	320	0.40×0.36	1500	78	6.1×10^3
122	J172519.5-342456	1160	0.37×0.37	5310	281	2.3×10^4
123	J172522.4-342150	230	0.53×0.17	880	46	7.0×10^3
124	J172522.8-342501	290	0.06×0.06	290	15	3.3×10^5
125	J172525.2-342338	350	0.27×0.26	990	36	8.1×10^3
126	J172525.8-341315	150	0.79×0.37	1340	71	1.8×10^3
127	J172527.2-342121	170	0.29×0.17	390	20	7.5×10^3
128	J172534.3-341831	220	0.48×0.31	1060	56	4.0×10^3
129	J172535.3-342021	180	0.42×0.16	540	29	6.7×10^3
130	J172535.9-342150	980	0.87×0.44	10730	542	9.5×10^3
131	J172538.2-343231	210	0.30×0.23	570	30	7.1×10^3
132	J172539.0-342916	870	0.41×0.22	2970	157	2.4×10^4
133	J172538.0-341349	270	0.41×0.34	1240	66	5.4×10^3
134	J172539.5-343129	210	0.19×0.17	380	20	1.4×10^4
135	J172541.0-343013	440	0.36×0.29	1640	86	9.9×10^3
136	J172541.5-342534	270	0.30×0.30	880	46	7.1×10^3
137	J172542.1-342233	720	0.37×0.30	2750	143	1.6×10^4
138	J172546.6-343031	290	0.38×0.30	1130	60	6.3×10^3
139	J172546.3-342232	210	0.36×0.14	530	27	1.0×10^4
140	J172546.2-341651	240	0.45×0.23	900	48	6.1×10^3
141	J172547.3-342941	410	0.63×0.38	2960	156	5.7×10^3
142	J172549.5-342144	310	0.65×0.22	1610	85	6.4×10^3
143	J172550.0-341917	170	0.41×0.19	530	28	5.4×10^3
144	J172551.7-341805	220	0.40×0.18	660	35	7.6×10^3
145	J172553.2-342241	290	0.65×0.31	1870	99	4.5×10^3
146	J172554.0-343305	320	0.53×0.30	1690	90	5.7×10^3
147	J172554.4-342946	190	0.46×0.30	900	47	3.7×10^3
148	J172600.2-341452	400	0.44×0.31	1830	97	7.7×10^3
149	J172601.4-343028	420	0.45×0.34	2100	111	7.5×10^3
150	J172601.2-341552	1500	0.23×0.17	3000	159	8.7×10^4
151	J172602.6-341344	180	0.58×0.22	840	42	4.0×10^3
152	J172603.2-341652	280	0.13×0.06	330	18	1.0×10^5
153	J172603.5-341239	310	0.46×0.33	1540	82	5.7×10^3
154	J172608.8-343130	150	0.27×0.25	410	22	5.0×10^3
155	J172610.1-341733	360	0.31×0.13	800	41	2.0×10^4
156	J172614.0-343216	280	0.35×0.20	810	43	9.7×10^3
157	J172620.5-344042	210	0.59×0.39	1440	76	2.9×10^3
158	J172620.0-343139	440	0.53×0.49	3310	175	5.6×10^3
159	J172623.3-343243	200	0.64×0.22	1000	53	4.0×10^3
160	J172631.6-340329	330	0.44×0.25	1290	68	7.9×10^3
161	J172641.6-343255	550	0.40×0.25	1990	104	1.3×10^4
162	J172647.1-343242	220	0.45×0.30	1000	53	4.5×10^3
163	J172651.6-340915	900	0.22×0.18	1780	94	5.2×10^4

Appendix A: Table

Table A.1. 24 μm flux and signpost of stellar activity.

Core number	$S^{\rm int}_{24\mu{\rm m}}$ (Jy	Maser/H II region	SSTGLMA coord. [5.8]–[8.0] [3.6]–[4.5] colors
3	1987.8 (5.9)	Maser/NVSS171702-362105	
7	3.82 (16)		G350.7120+01.0239 0.564 1.220
8	3.94 (7.7)		
9	0.57 (7.5)		
10	0.42 (4.9)		
12	0.19 (5.1)		G350.6054+00.6804 0.756 1.807
15	0.11 (13.1)		
17	0.22 (8.6)		
18	8.72 (11)		
19	0.025 (4)		G350.9596+00.7395 0.43 1.246
29	392.7 (16)	Maser	
30	–	Maser	
38	204.1 (6.8)	Maser/NGC 6334A/NVSS172019-355453	
39	2.69 (5.7)		
46	30.7 (13.5)		
47	–	NGC 6334C	
51	422.1 (23)	NGC 6334D/NVSS172044-354917	
58	0.26 (11.1)		
61	1.05 (5.8)		
62	927.9 (0.2)	Maser/NGC 6334F/[WBH2005]351.417+0.644	
63	0.61 (14)	Maser/NGC 6334I(N)	
64	0.50 (4.2)		G351.4968+00.6903 0.791 2.137
65	1.43 (12.7)		
67	0.86 (6)		G351.6464+00.7671 1.569 2.859
72	7.08 (3.8)		G351.5888+00.5922 0.7750 1.688
73	–	(NVSS172138-353227)	
76	0.68 (6.6)		
78	0.32 (8.6)		
79	0.16 (7)		
81	3.19 (13.5)		
82	0.051 (7)		
84	0.046 (1)		G352.3865+00.8242 1.409 1.996
85	52.6 (4.5)	[WBH2005]352.493+0.795	
86	0.028 (2.5)		
87	0.080 (16.2)		
88	0.20 (12.5)		
89	0.33 (15)		
90	0.57 (21.6)	(NVSS172339-341400)	
91	1.07 (7.8)		
92	–		G353.1111+01.0751 0.522 0.98
98	0.33 (14)		G353.0837+00.9932 1.116 1.816
109	140.8 (13.1)	[WBH2005]353.202+0.922	
110	1754.5 (11)	NVSS172445-341032	
111	–	[WBH2005]353.208+0.907	
115	–	(NVSS172500-341225)	
122	0.73 (8.3)		
125	–	[WBH2005]353.094+0.670	
130	206.2 (19.6)	NVSS172535-342140	
147	16.7 (10)		
148	–	Maser	
151	–	(NVSS172603-341357)	
152	–		G353.2549+00.6219 0.68 0.111
154	0.080 (12)		
158	0.39 (11.9)		
160	0.028 (8.8)		
163	–	Maser	

Notes. Column 1: core identification number. Column 2: measured 24 μm flux (see Sect. 4.1.3). In parentheses we indicate the difference in position between the MIPS source and the SIMBA peak (in arcsecondes). Column 3: maser and/or a radio counterpart (in this case the identification of the radio source is given; radio sources in parentheses indicate that the core is at the border of the radio source but not considered as directly associated). Column 4: GLIMPSE catalogue archive designation (e.g. SSTGLMA G350.7120+01.0239) of the associated GLIMPSE source followed by the [5.8]–[8.0] and [3.6]–[4.5] colors (from magnitudes given in the IRAC/GLIMPSE catalogue).